UNIVERSITY OF OKLAHOMA

GRADUATE COLLEGE

INTEGRATION OF PHASE CHANGE MATERIAL-BASED THERMAL ENERGY STORAGE IN AIR DISTRIBUTION SYSTEMS TO INCREASE BUILDING POWER FLEXIBILITY

A THESIS

SUBMITTED TO THE GRADUATE FACULTY

in partial fulfillment of the requirements for the

Degree of

MASTER OF SCIENCE

By

PHILANI GIFT HLANZE
Norman, Oklahoma
2020

INTEGRATION OF PHASE CHANGE MATERIAL-BASED THERMAL ENERGY STORAGE IN AIR DISTRIBUTION SYSTEMS TO INCREASE BUILDING POWER FLEXIBILITY

A THESIS APPROVED FOR THE
SCHOOL OF AEROSPACE AND MECHANICAL ENGINEERING

BY THE COMMITTEE CONSISTING OF

Dr. Jie Cai, Chair

Dr. Hamidreza Shabgard

Dr. Li Song

Acknowledgements

I would like to thank my Faculty Advisor, Dr. Cai, who welcomed me to his research group as an undergraduate student and mentored me through my master's degree studies. His guidance has helped me to develop my skills as a researcher, and I look forward to working with him in my PhD studies as well. I would like to thank my committee members, Dr. Song and Dr. Shabgard, who contributed to my intellectual growth through their courses and provided a critical viewpoint for my research. I would like to thank my lab mates Aly Elhefny and Zhimin Jiang, who's assistance was vital to my completion of experiments and numerical simulations. I would also like to thank the undergraduate research assistants who helped me with my experimental set up. I would like to thank the School of Aerospace and Mechanical Engineering staff for their support throughout my studies. I would like to thank my family, especially my parents, whose sacrifices allowed me to pursue an education at Waterford KaMhlaba UWCSA and subsequently, OU. This achievement is yours as much as it is mine. I would like to thank my friends who provided support throughout this journey. Lastly, I would like to thank my partner, Norma Lilia Ruiz Cruz, whose companionship helped me to push through the tough times that I encountered and appreciate the joyful moments that I experienced as well.

Table of Contents

List of Tables

List of Figures

Abstract

Thermal energy storage is one of the many strategies that are effective in alleviating the electrical power supply and demand imbalance issues on the electric grid, and buildings are a good place to implement such storage solutions because of their high electricity consumption. This thesis presents a novel energy storage solution by incorporating phase change material (PCM) in the building supply-air duct. The in-duct PCM storage has various advantages compared to PCM-integrated walls including more effective heat transfer (forced convection and greater temperature differentials). During off-peak hours, the system runs at a supply-air temperature below the material's solidification point to charge the PCM with cooling energy. During on-peak hours, a higher supply-air temperature is utilized so that the stored energy can be discharged into the supply-air. This shifts a portion of building's cooling load from the on-peak hours to the off-peak hours. A numerical model for the melting and solidification of PCM in the duct was developed and modified using experimental data. Whole building energy simulations were conducted by coupling the PCM numerical model with EnergyPlus' DOE prototypical building model in a Simulink co-simulation platform. Simulations were performed for three cities in different climate zones over a three-month cooling season (June to August) and the PCM storage reduced the on-peak energy consumption by 20-25%. The electricity cost and payback period were determined using current time-of-use electricity rates.

1. Introduction

While the introduction of renewable energy sources has provided an alternative to fossil fuels and their associated greenhouse gas emissions, their limited window of availability (particularly solar energy) has resulted in the rapid ramping of fossil fuel power plants to make up for the energy shortfall during the evening hours [1]. As a result, a lot of stress is put on these plants over a short period of time, which might shorten their lifespan and lower the overall generation efficiency. Thus, there is a need to shift the demand on the electricity grid to off-peak hours and create a more balanced daily supply and demand. In the US, commercial buildings and residential homes account for about 40% of the total energy consumption, and in commercial buildings, 32% of that energy is consumed by the Heating, Ventilation and Air-Conditioning (HVAC) systems [2]. Furthermore, the square footage of commercial buildings increased by 78% between 1978 and 2008. This trend indicates that buildings and their HVAC systems will continue to be a significant contributor to the US energy consumption. This makes commercial buildings an attractive area to implement energy savings and peak load reduction strategies.

Thermal energy storage (TES) is one of the many strategies that are effective in alleviating the electrical power supply and demand imbalance issues on the electric grid, and buildings are a good place to implement such storage solutions because of their high electricity consumption. TES can be implemented in buildings using sensible heat or latent heat [3]. Sensible heat storage involves using the building's thermal mass as a thermal battery by increasing or decreasing the temperature of the building envelope. Latent heat storage involves using a phase change material's (PCM) latent heat of fusion to store energy in the material during the phase change process.

The proposed PCM latent energy storage solution is displayed in Figure 1.1. The PCM will be located in the supply-air duct in order to take advantage of the forced convection heat transfer provided by the moving air. The supply-air temperature (SAT) will be lowered to initiate the PCM solidification (PCM charging) and store "cooling" energy in the PCM. Once the PCM has solidified, the SAT is increased to initiate the PCM melting process (PCM discharging). The PCM charging process is conducted during the off-peak hours and the PCM discharging process is conducted during the on-peak hours. This increases the HVAC cooling load during the PCM charging and decreases it during the PCM discharging. When implemented with time-of-use (TOU) electricity rates, which have a higher electricity price during on-peak hours and lower electricity cost during off-peak hours, the building electricity cost can be effectively reduced.

The objective of this thesis is to evaluate the energy cost savings and peak electric demand reduction that can be achieved installing PCM in the supply air duct of the HVAC system. This objective will be achieved by formulating a model for the melting and solidification of PCM in the duct, conducting a whole building simulation for a PCM-equipped medium office building in different climate zones using an EnergyPlus-Simulink co-simulation platform, and calculating the energy cost savings and payback period using current TOU rates.

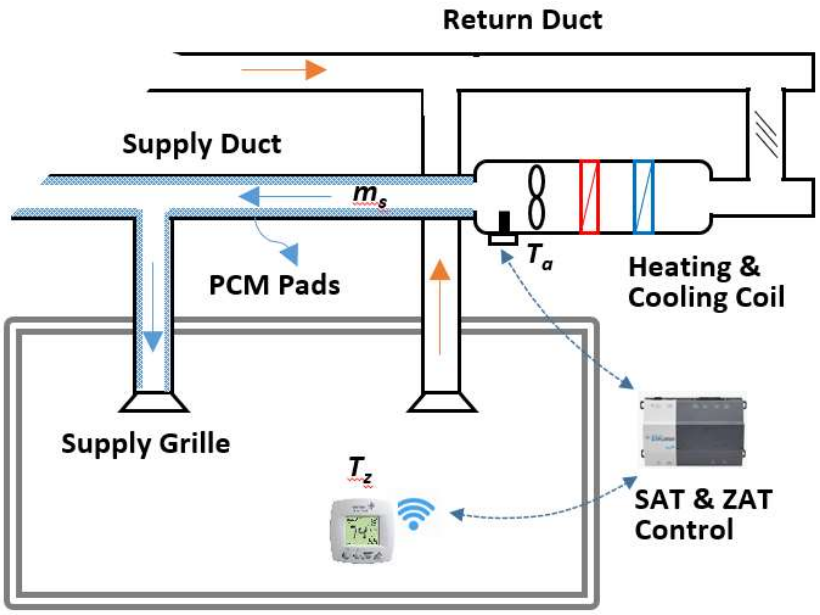

Figure 1.1. Proposed PCM storage location

2. Literature Review

PCM undergo solid-liquid phase transitions at a temperature within the operating temperature of a thermal energy system [4]. They can be classified into organic, inorganic and eutectic [5]. Organic PCMs are non-toxic, non-corrosive and have good thermal stability; however, they have low thermal conductivity which leads to high phase change times [6]. While inorganic PCMs have high thermal conductivity, they are more corrosive, toxic and have lower chemical and thermal stability, which makes them less suitable to be placed in the supply air duct.

The use of PCM as latent heat storage has previously been investigated in many studies. Iten et al. [3] conducted a review of free cooling TES and PCM incorporated in the building envelope to increase the building's thermal mass. For PCM incorporated in the building envelope, the energy storage is driven by the increase or decrease in the outdoor or indoor temperatures, which initiates the melting or solidification process. Safari et. al [7] investigated the implementation of PCM in roof and wall construction using the Fanger comfort model to control HVAC thermostat operation in Madrid's climate zone. They found that a PCM with 27 °C melting temperature resulted in the highest energy savings potential, and 5 mm thick modules resulted in a maximum of 16% annual energy savings and a minimum 6.38-year payback period for the office schedule. Neeper [8] investigated the thermal dynamics of a wallboard impregnated with PCM. The study found that the maximum diurnal energy storage occurs at a value of the PCM melt temperature that is close to the average room temperature in most circumstances. The diurnal storage achieved in practice may be limited to a range of 300–400 kJ/m^2, even if the wallboard has a greater latent capacity. However, the investigation used a pre-determined hourly room temperature profile, and the effect of the PCM on the room temperature was not considered. Sleiti and Naimaster [9] investigated the building energy performance of recently developed organic

(fatty acid based) PCM products in ceiling constructions for a simulated quick service restaurant building model located in Atlanta, GA. PCM was added in the ceiling, in between the gypsum board and attic floor frame and insulation. The PCM cases considered were not able to achieve any changes in the zone air temperature that would translate to significant HVAC energy savings. In an experimental and numerical study, Athienitis et al. [10] impregnated PCM in gypsum board and inserted it in the inside wall lining of a full-scale outdoor test room. They observed reasonable agreement in the simulation and experimental results, which demonstrated that a maximum room temperature reduction of about 4 °C during the daytime. Lin et al. [11] studied an electrical floor heating system with ductless air supply and shape-stabilized PCM. The study demonstrated the electrical load shifting capabilities from the on-peak to off-peak periods; however, the economic benefits might be offset by implementing this novel under-floor heating system. PCM has also been incorporated in window panes and shutters to minimize solar heat gains through the window [12] [13]. One of the limitations for PCM TES incorporated in the building envelope is that the fluctuations in the zone temperature required to perform energy storage can lead to discomfort for the occupants [14] [15]. The air-to-PCM heat transfer is low due to the reliance on natural convection and the small temperature difference limits the effectiveness and heat penetration depth.

Free cooling TES has been previously investigated, and it involves using the stored cooling potential of cold night-time air to cool the indoor space during the day [16]. At night, cold outdoor air is circulated through the PCM storage unit, which solidifies the PCM and stores “cooling energy” in it. During the day, hot air from the room is circulated through the PCM storage unit, which melts the PCM and delivers cooled air to the interior space. Zalba et al. [17] designed an experimental installation to study a PCM free cooling system using a flat plate heat exchanger.

Their analysis showed that the main parameters with significant influence on the solidification and melting processes are the thickness of the encapsulation, the inlet temperature of the air, the air flow rate, and the interaction thickness and temperature. Mosaffa et al. [18] performed a numerical investigation on the performance enhancement of a free cooling using TES unit for multiple PCMs. They modeled the PCM melting and solidification using the heat capacity method and investigated the effect of the PCM slab length and thickness, and the air passage width using an energy optimized method. They demonstrated that a system that utilized a PCM combination of $CaCl_2 \cdot 6H_2O$ and Rubitherm RT25, an optimum air channel width of 3.2 mm, length of 1.3 m and PCM slab thickness of 10 mm can achieve an optimum COP of 7.0 in Tabriz, Iran. Anisur et al. [19] investigated analytically and experimentally a shell and tube latent heat storage system using heptadecane with melting point 22.33 °C. The study found that a higher inlet temperature led to a higher COP, and the COP was to be 4.16 for an inlet temperature of 34.5 °C, tube inner radius of 5.35 mm and thickness of 1 mm. Osterman et al. [20] investigated the performance of a latent heat storage unit experimentally and numerically using Fluent. The investigation was conducted over the period of a year: in the summer, free cooling was stored in the PCM using cold night air, and in the winter, free heating was stored in the PCM during the day using a solar air collector and released to the indoor space at night. The study found that the largest winter savings occurred in March because of the availability of heat in larger quantities, and the largest cooling storage occurred in July and August because of the larger temperature fluctuations between day and night. Takeda et al [21] investigated the reduction of the ventilation load during summer in various Japanese cities by installing a packed bed of PCM granules in the supply-air ventilation duct. When the outdoor air temperature is less than room air, two separate streams of outdoor air flow into the room and through the PCM bed to simultaneously charge the PCM and cool room. The air that

leaves the PCM section is exhausted to the outdoor environment because it has gained heat from the PCM. When outdoor air temperature is higher than room air, outdoor air only passes through PCM bed and goes into room. The maximum ventilation load reduction was determined to be 62.8% in Kyoto; however, in the study the indoor air temperature was kept constant (26 °C) and heat transfer through the building walls was not considered. Yanbing et al [22] analyzed the thermal behavior of a Night Ventilation with PCM Packed Bed Storage (NVP) and determined convective heat transfer coefficients of 12 to 19 $W/m^{2}\cdot°C$ and air flow resistance through the PCM of less than 20 Pa. Free cooling can also take advantage of geocooling in climates where the ground temperature is lower than room temperature. McKenna et al [23] explores the potential for using geocooling or 'geothermal free cooling' in combination with TES to reduce the energy and carbon impact of cooling in a small, lightweight commercial building located in a Mediterranean climate. A mathematical model was developed and validated experimentally and implemented in TRNSYS. The geocooling alone was able to meet 84% of the cooling load, but the inclusion of PCM storage increased the capacity to 99%. Free cooling TES is attractive because it makes affective use of "free" energy source, but its main disadvantage is the requirement for bypass duct/dampers to allow for the active control of the charging/discharging periods and prevent overcooling of the indoor spaces.

PCM TES has also been implemented in solar cooling systems to provide cooling during solar energy's unavailability [16]. Helm et al. [24] studied the benefits of a solar-driven absorption cooling system that uses a PCM storage unit and a dry air cooler instead of a conventional wet cooling tower in the heat rejection circuit. They found that energy consumed by the heat rejection can be shifted to night-time or off-peak hours, which have lower ambient temperatures. Helm et al. [25] performed another study of a solar-driven absorption cooling system with a PCM TES and

dry air cooler heat rejection circuit that consisted of four pilot installations between 7 kW and 90 kW nominal cooling capacity and latent heat storages between 80 kWh and 240 kWh. Annual in situ measurement data demonstrate an increase off the seasonal energy efficiency ratio (SEER) for cooling up to 11.4, and simulations under different climatic conditions indicate a rise in efficiency up to 64% compared to a system with solely dry re-cooling. Belmonte et al. [26] performed a feasibility study for the integration of a dry air cooler and PCM TES in the heat rejection circuit of absorption solar cooling systems for the residential sector in Spain. They found that the chiller's COP is deteriorated by 7-13%, and the evaporator's total cooling energy is decreased by 21-38% when compared to a conventional wet cooling tower; however, the system efficiency is improved by 50%. While the implementation of PCM TES can improve the efficiency of solar cooling systems, this application is limited to systems that already use solar energy, and the capital costs of converting to solar cooling systems will reduce the potential energy cost savings.

Dedicated cold storage using ice is a latent heat thermal energy storage solution with validated field deployments [27] [28]. Ice can be stored in tanks and employed to shift the energy demand from on-peak to off-peak hours [29]. In larger applications, summer heat is stored to provide space heating during the winter, and winter cool is stored to provide space cooling in the summer [30]. Yau and Lee [31] conducted a simulation case study using TRNSYS and Typical Meteorological Year (TMY) weather data for Kuala Lumpur. They employed an ice-slurry cooling storage system in a library building, which increased the cumulative energy consumption by 20% from the existing system. However, the shifting of the chiller load to the off-peak period led to energy cost savings of about 24%. Morgan and Krarti [32] investigated the peak cooling shifting capabilities of ice thermal storage in a Colorado elementary school. A 50 ton scroll compressor charges three ice tanks during the night, and the stored cooling is used during the day while the

chiller is kept in assist mode to handle unexpected cooling loads. They found that the ice storage system could achieve annual energy cost savings of around 47% due to a utility rate of $0.0164/kWh and a demand charge of $11.24/kW. Despite the energy cost savings potential of ice cold storage systems, their applications are limited to large commercial design due to the complicated design, high capital investment and maintenance costs.

The PCM TES solution proposed in this thesis attempts to address some of the issues pointed out in the aforementioned studies. By placing the PCM in the supply air duct, the heat transfer is driven by forced convection, which should improve the rate of thermal penetration compared to the passive systems. The supply-air temperature can be adjusted to provide a high enough temperature difference between the air and the PCM, and at the same time still ensure that enough cooling is being provided to the building zones. The solution does not require any bypass duct or dampers, so it is easier to retrofit than most of the free cooling solutions.

3. Whole Building Simulation

In this section, the PCM model and EnergyPlus-Simulink co-simulation platform used to perform the whole building simulations are described.

3.1 PCM Model

The PCM is installed into the supply-air duct by mounting it on the interior surfaces of the vertical and horizontal duct walls, as displayed in Figure 3.1. Heat is transferred between the air and PCM through the PCM casing. The duct wall is assumed to be well insulated with external duct insulation and no heat is lost through the duct wall.

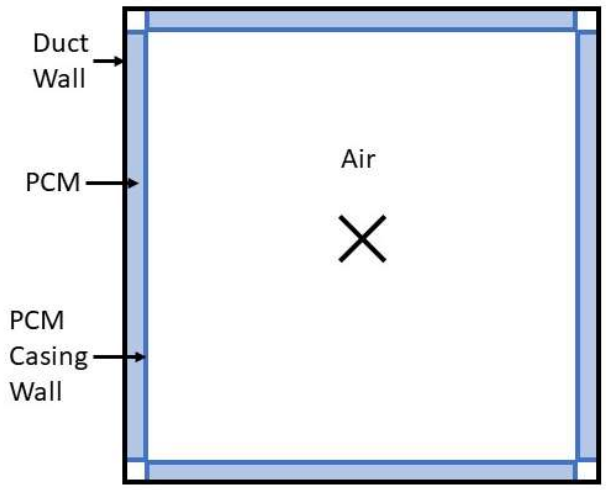

Figure 3.1. Cross-sectional view of PCM in HVAC Duct

The PCM model used in the whole building simulation is adapted from the Enthalpy method [33]. The heat transfer in the PCM is modeled as a one-dimensional conduction-controlled, two-region melting problem in a finite slab, which means that heat transfer is only considered in one direction and the natural convection heat transfer effects in the PCM are not considered. The

density of the solid and liquid phases is assumed to be equal ($\rho_s = \rho_l = \rho$), and the governing equation is

$$\rho \frac{\partial h}{\partial t} = \frac{\partial}{\partial x}\left(k \frac{\partial T}{\partial x}\right) \tag{3.1}$$

which is valid for the entire PCM region. The initial enthalpy is defined as

$$h(T) = \begin{cases} c_{p_s}(T - T_m) & T < T_m \\ 0 & T = T_m, \text{fully solidified} \\ h_{sl} & T = T_m, \text{fully melted} \\ c_{p_l}(T - T_m) + h_{sl} & T > T_m \end{cases} \tag{3.2}$$

where h_{sl} is the latent heat of the PCM, T_m is the PCM melting temperature, c_{pl} is the liquid specific heat of the PCM and c_{ps} is the solid specific heat of the PCM. The PCM is initially either fully solid or liquid, but when the PCM is melting/solidifying, h is between 0 and h_{sl}. The initial PCM thermal conductivity is assigned according to the initial phase:

$$k(T) = \begin{cases} k_s & T \le T_m, \quad h(T) \le 0 \\ k_l & T \ge T_m, \quad h(T) \ge h_{sl} \end{cases} \tag{3.3}$$

where k_s and k_l are the solid and liquid thermal conductivities, respectively. The governing equation is discretized using a forward difference in time and central difference in space as follows:

$$\rho \frac{h_j^{n+1} - h_j^n}{\Delta t} = \frac{k_{j+\frac{1}{2}}\left(T_{j+1}^n - T_j^n\right) - k_{j-\frac{1}{2}}\left(T_j^n - T_{j-1}^n\right)}{(\Delta x_{PCM})^2} \quad j = 2, \ldots, N-1 \tag{3.4}$$

where the location and time are represented by j and n, respectively. Figure 3.2 displays how the nodes in the PCM are arranged. The thermal conductivities at the half-grid, $k_{j+½}$ and $k_{j-½}$, are calculated using the harmonic mean method:

$$k_{j+\frac{1}{2}} = \frac{2k_j k_{j+1}}{k_j + k_{j+1}} \tag{3.5}$$

$$k_{j-\frac{1}{2}} = \frac{2k_j k_{j-1}}{k_j + k_{j-1}} \tag{3.6}$$

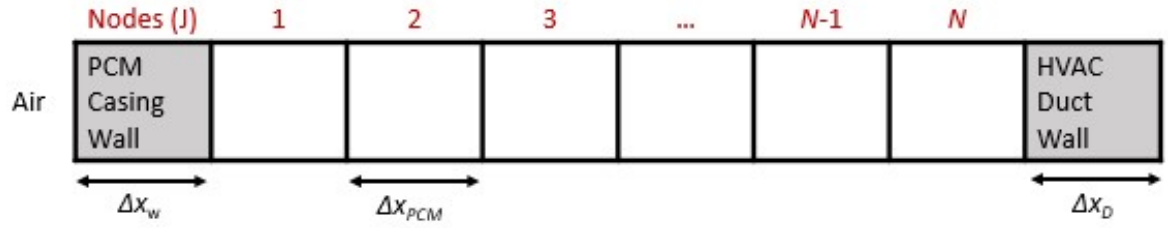

Figure 3.2. PCM model node arrangement

When rearranged to solve for the enthalpy at the $(n+1)^{th}$ timestep, equation 3.4 becomes

$$h_j^{n+1} = \frac{\Delta t}{\rho(\Delta x)^2}\left(k_{j+\frac{1}{2}}T_{j+1}^n + k_{j-\frac{1}{2}}T_{j-1}^n\right) + \left(h_j^n - \frac{\Delta t\left(k_{j+\frac{1}{2}} + k_{j-\frac{1}{2}}\right)}{\rho(\Delta x)^2}T_j^n\right) \tag{3.7}$$

The enthalpy at node N, which is adjacent to the duct wall, is calculated using

$$h_N^{n+1} = \frac{\Delta t}{\rho(\Delta x_{PCM})}\left(\frac{k_{N-\frac{1}{2}}(T_{N-1}^n - T_N^n)}{\Delta x_{PCM}} - \frac{T_N^n - T_D^n}{\frac{\Delta x_D/2}{k_D} + \frac{\Delta x_{PCM}/2}{k_N}}\right) + h_N^n \tag{3.8}$$

where T_D is the duct temperature, Δx_D is the duct thickness, k_D is the duct thermal conductivity and A is the area perpendicular to the heat flow. Once the enthalpy at each node is determined, the temperature is found using

$$T_j^{n+1} = \begin{cases} T_m + \dfrac{h_j^{n+1}}{c_{ps}} & h_j^{n+1} \le 0 \quad (solid) \\ T_m & 0 < h_j^{n+1} < h_{sl} \quad (interface) \\ T_m + \dfrac{h_j^{n+1} - h_{sl}}{c_{pl}} & h_j^{n+1} \ge h_{sl} \quad (liquid) \end{cases} \tag{3.9}$$

The heat transfer into the duct wall is calculated as

$$m_D c_D \frac{T_D^{n+1} - T_D^n}{\Delta t} = \frac{T_N^n - T_D^n}{\frac{\Delta x_D/2}{k_D A} + \frac{\Delta x_{PCM}/2}{k_{PCM} A}} \tag{3.10}$$

3.2 Air-to-PCM Heat Transfer

The air-to-PCM heat transfer was modeled using the convection correlations for internal turbulent flow, specifically the *Dittus-Boelter correlation* [34]. The Nusselt number is calculated using

$$Nu_D = 0.023 Re_D^{4/5} Pr^n \tag{3.11}$$

where Re_D is the Reynolds number and Pr is the Prandtl number. The Prandtl number is calculated using

$$Pr = \frac{c_{pa}\mu}{k_a} \tag{3.12}$$

where c_{pa} is the specific heat of the air, μ is the dynamic viscosity and k_a is the thermal conductivity of the air. The Reynolds number is calculated using

$$Re_D = \frac{\rho_a v D_h}{\mu} \tag{3.13}$$

where ρ_a is the air density, v is the air velocity, D_h is the hydraulic diameter. The hydraulic diameter is calculated using

$$D_h = \frac{4A_c}{P} \tag{3.14}$$

where A_c is the duct cross-sectional area and P is the wetted perimeter. The convective heat transfer coefficient is calculated as

$$h = \frac{Nu_D k_a}{D_h} \tag{3.15}$$

The heat transfer through the PCM casing wall is calculated using

$$m_w c_w \frac{T_w^{n+1} - T_w^n}{\Delta t} = \underbrace{\frac{T_{air}^n - T_w^n}{\frac{1}{hA} + \frac{\Delta x_w/2}{k_w A}}}_{q_{\text{in}}} - \underbrace{\frac{T_w^n - T_1^n}{\frac{\Delta x_w/2}{k_w A} + \frac{\Delta x_{PCM}/2}{k_{PCM} A}}}_{q_{\text{out}}} \tag{3.16}$$

where m_w is the mass of the PCM casing wall, c_w is the specific heat of the PCM casing wall, T_w is the temperature of the PCM casing wall, T_{air} is the air temperature, Δx_w is the wall thickness, k_w is the wall thermal conductivity and T_1 is the temperature of the PCM node adjacent to the wall. The enthalpy of the first PCM node is calculated using

$$h_1^{n+1} = \frac{\Delta t}{\rho(\Delta x_{PCM})}\left(\frac{q_{out}}{A} - \frac{k_{1+\frac{1}{2}}(T_1^n - T_2^n)}{\Delta x_{PCM}}\right) + h_1^n \tag{3.17}$$

where

$$q_{out} = \frac{T_w^n - T_1^n}{\frac{\Delta x_w/2}{k_w A} + \frac{\Delta x_{PCM}/2}{k_{PCM} A}} \tag{3.18}$$

The length of the duct is divided into different sub-sections and the PCM model is evaluated at each sub-section in a sequence from the inlet to the outlet sub-section. The outlet air of the previous subsection is considered the inlet air of the next section. Figure 3.3 displays the flow of air and energy in each duct subsection. The temperature of the air entering the next duct sub-section is calculated using

$$T_{out} = T_{in} - \frac{q_{in}}{\dot{m}_a c_{pa}} \tag{3.19}$$

where $\dot{m}_a$ is the air mass flow rate and

$$q_{in} = \frac{T_{air}^n - T_w^n}{\frac{1}{hA} + \frac{\Delta x_w/2}{k_w A}} \tag{3.20}$$

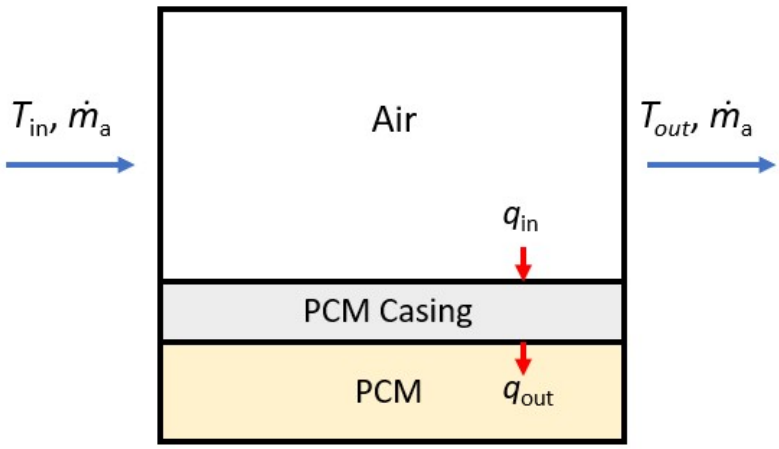

Figure 3.3. Lengthwise view of heat transfer in one duct section

3.3 PCM Experiment

3.3.1 Experiment Setup

The objective of the small-scale experiment is to determine the heat transfer enhancement of adding fins to the PCM module. The test was conducted by placing a 1" deep acrylic tray that is filled with PCM and covered by a finned aluminum sheet downstream of an Air Handling Unit (AHU) as displayed in Figure 3.4. The AHU blew air over the PCM module; the supply air temperature was measured using an array of 5 thermocouples suspended in the duct and the airflow rate was measured using a hot-wire anemometer. Inside the PCM tray, two columns are mounted to the bottom of the tray to suspend thermocouples at depths of 0.25", 0.5", and 0.75". Two thermocouples were also placed on the inside surfaces of the tray bottom and the aluminum fins. The dimensions of the finned aluminum lid are displayed in Figure 3.5 and Table 3.1. The PCM used in the experiment was PureTemp 15, which is a biobased PCM with a nominal melting point of 15˚C [35]. The PCM thermal properties are displayed in Table *3.2*.

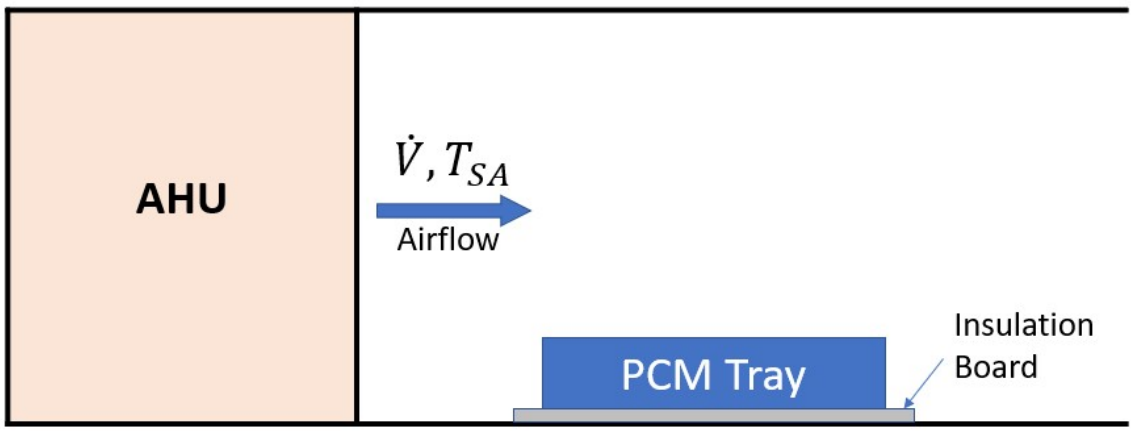

Figure 3.4. Placement of PCM module in HVAC Duct

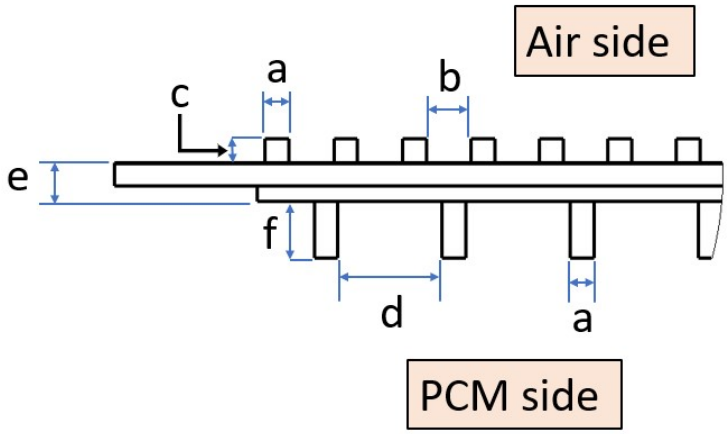

Figure 3.5. Dimensions of the finned aluminum lid

Table 3.1. Aluminum fin dimensions

Dimension	Value (in.)
a	0.100
b	0.188
c	0.100
d	0.406
e	0.163
f	0.238

Table 3.2. PCM thermal properties

Thermal Property	Value
T_m (°C)	15
h_{sl} (J/kg)	182000
ρ (kg/m^3)	905
c_{pl} (J/kg·K)	2560
c_{ps} (J/kg·K)	2250
k_l (W/m·K)	0.15
k_s (W/m·K)	0.25

3.3.2 Experiment Parameters

The AHU's operating parameters were controlled and measured using a LabVIEW program. The experiment was conducted in two stages: the first stage consisted of solidifying the PCM that was initially in the liquid phase, and the second stage consisted of melting the PCM directly after the first stage. During the first stage, the supply-air temperature was set at 9 °C, and the airflow rate was set to 700 CFM. During the second stage, the supply-air temperature was set to 19 °C, and the airflow rate was set to 1475 CFM to achieve a similar cooling rate to the first stage. Figure 3.6 displays the variation of the test parameters during the experiment.

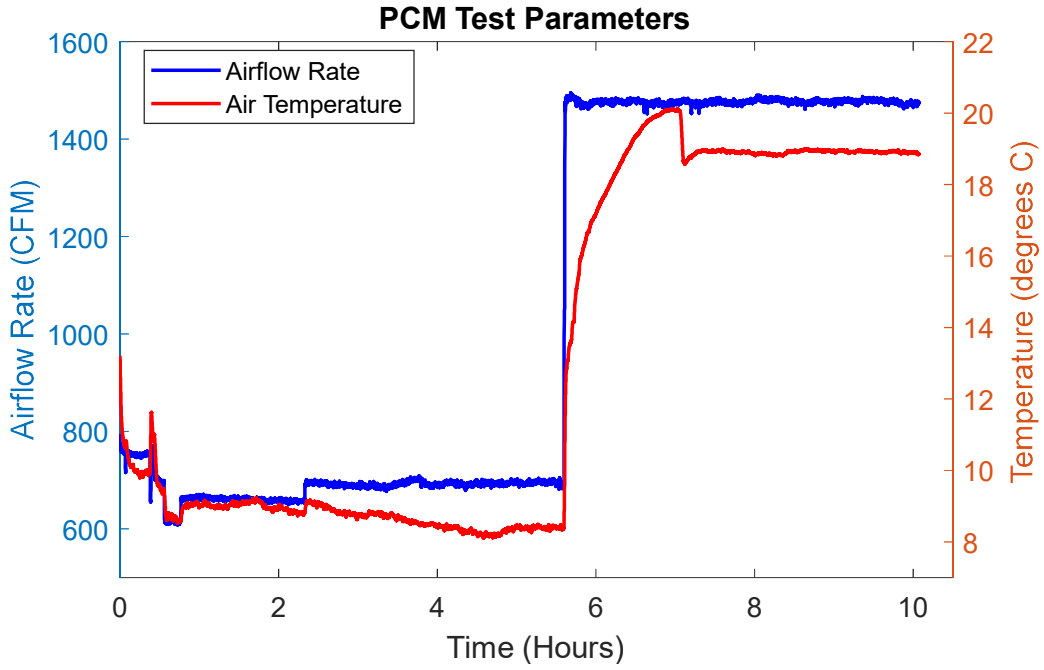

Figure 3.6. PCM Experiment Test Parameters

3.3.3 Experiment Results and Analysis

The variation of PCM temperatures is displayed in Figure 3.7. Initially, the PCM temperature decreases as it loses heat to the colder overflowing air. The PCM that was used has an advertised melting temperature of 15 °C, but the PCM's temperature dropped to around 12.5

°C and began to rise again due to the subcooling effect, which causes the PCM temperature drops below the melting temperature while the initial solid crystals are being formed.

The first stage lasted for 5.6 hours and at this point between 75% and 50% of the PCM had solidified. This can be deduced from the rapid decrease in the PCM temperature at the 0.5” height, while the PCM temperature was slightly decreasing at the 0.25” height. This is confirmed visually in Figure 3.8, which shows the solid PCM at the top and the solid-liquid interface below halfway depth. Once stage 2 began, the PCM temperatures began to increase as heat was being gained from the hot air. Initially, the bottom and 0.25” high thermocouples recorded an increase in temperature, but the temperature quickly decreased and started rising slowly. This was caused by taking the tray out for inspection at the end of the first stage, which exposed the bottom of the tray to the warmer room air. This effect is displayed in Figure 3.9 where a solid layer can be seen on the bottom of the tray. After 4.4 hours, the PCM had fully melted, which is indicated by the rapid increase in temperature of the bottom thermocouple and the absence of solid crystals in Figure 3.10.

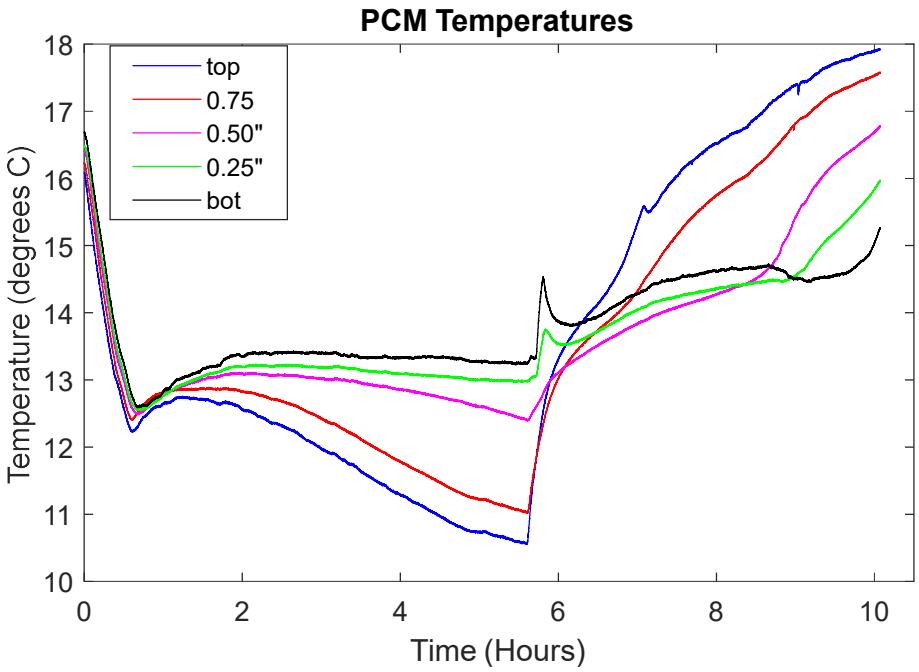

Figure 3.7. PCM temperature profile over the duration of the experiment

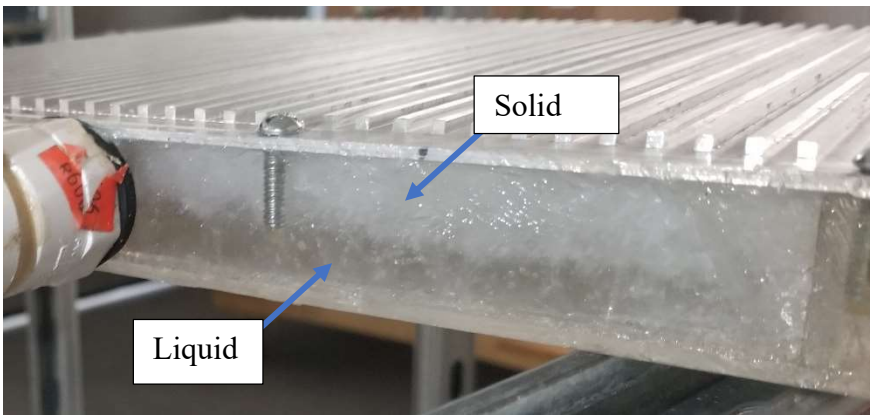

Figure 3.8. PCM Solidification at the end of Stage 1

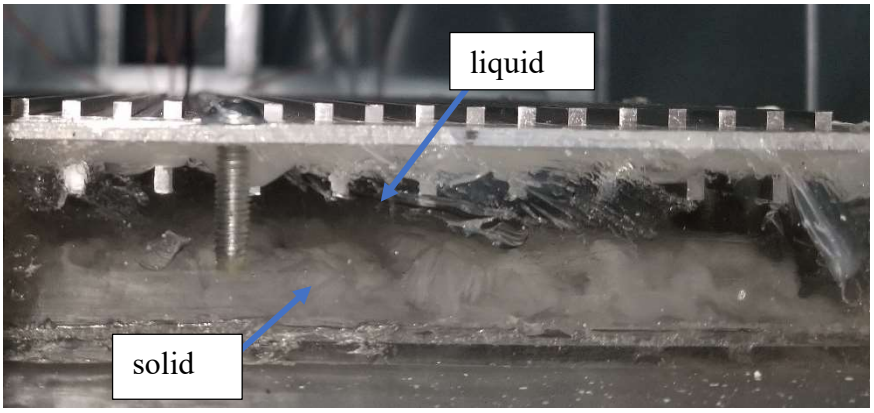

Figure 3.9. PCM melting at 3 hours after stage 2 commenced

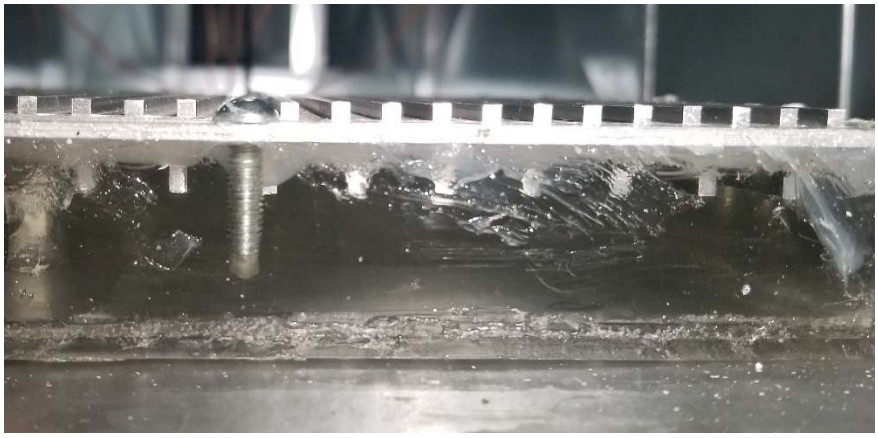
Figure 3.10. Fully melted PCM at the end of stage 2

The experimental data was used to estimate a heat transfer enhancement factor to the PCM model that represents the addition of fins. The three parameters chosen to apply the enhancement factor are the air-side convective heat transfer coefficient and the solid and liquid PCM thermal conductivities, since the addition of fins enhances both the air-to-PCM convection and in-PCM conduction heat transfer. The factor was applied using a scalar multiplier, z, where

$$h_{air,enhanced} = h_{air} * z$$
$$k_{s,enhanced} = k_s * z \quad (3.21)$$
$$k_{l,enhanced} = k_l * z$$

The factor z was determined using MATLAB's *nlinfit* function to perform a nonlinear curve fitting. The experimental data for each PCM depth is concatenated into one vector and the temperature reported by the PCM model at the respective depths is also concatenated to form the two datasets that are fitted. Figure 3.11 displays the comparison of the experiment data and the PCM model's predicted temperature at each depth. The melting temperature used in the PCM model was changed to 13.5 °C to better match the measured dynamics. The PCM model was unable to reflect the rate at which the PCM melted during the experiment. The top temperature was the only temperature that reached the melting point during the first stage predicted by the model. However, it only experienced a rapid decrease in temperature (which signifies a complete phase change at that point) after 5 hours. The rest of the PCM temperature remained above the melting temperature for the duration of stage 1, which show that they had not undergone phase change, and does not match the rate of solidification recorded in the experiment.

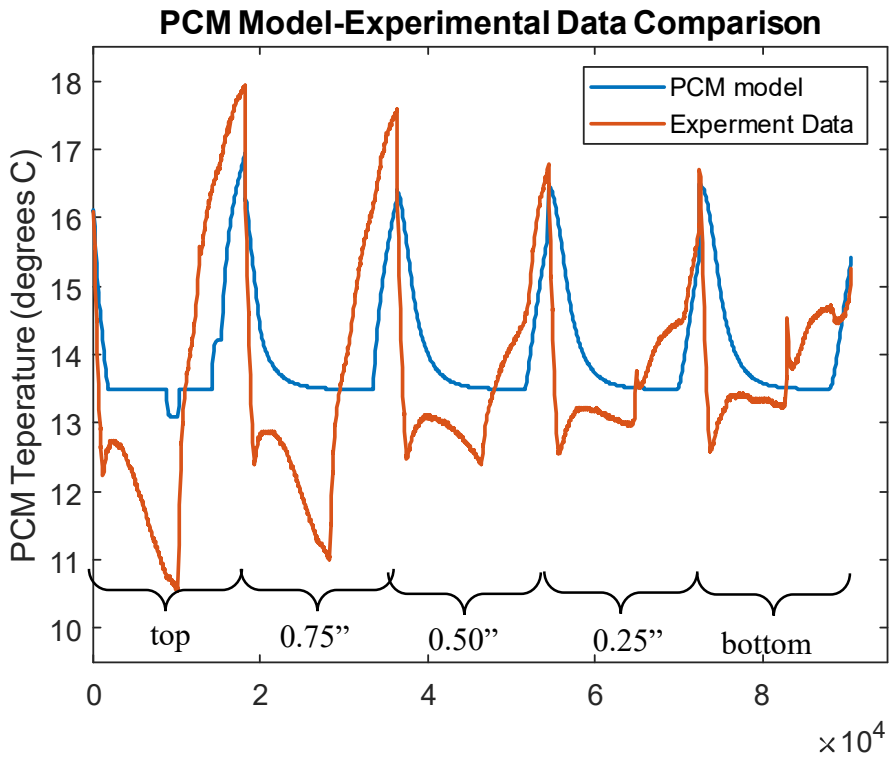

Figure 3.11. PCM Temperature predicted by the PCM model before the factor z is applied

The enhancement factor z was estimated to be 8.5, and the resulting temperature distribution simulated by the corrected PCM model is shown in Figure 3.12. After z is applied, the PCM model is now much closer to the experimental data, although it is not a complete match. The sources of mismatch are the non-ideal phase change due to PCM subcooling, which is not captured by the Enthalpy method. The single enhancement factor limits how close the PCM model is fitted to the experimental data because it assumes that the air-to-PCM heat transfer enhancement is equal to the internal PCM heat transfer enhancement. Also, the fin depth is lower than the PCM thickness, which causes a non-uniform conductivity enhancement in the PCM.

For the top temperature, the PCM model undergoes rapid solidification and melting at the beginning of the first and second stages, but the final temperature was higher for stage 1 and lower for stage two. This trend is similar for the other temperature nodes. The duration of the melting

and solidification processes are similar but there is a difference in the final temperature when the phase change is complete. Since the focus of the simulation is latent energy storage, the tracking the phase change process is more important than the sensible heating process. In the whole building simulations, the enhanced PCM heat transfer model was used.

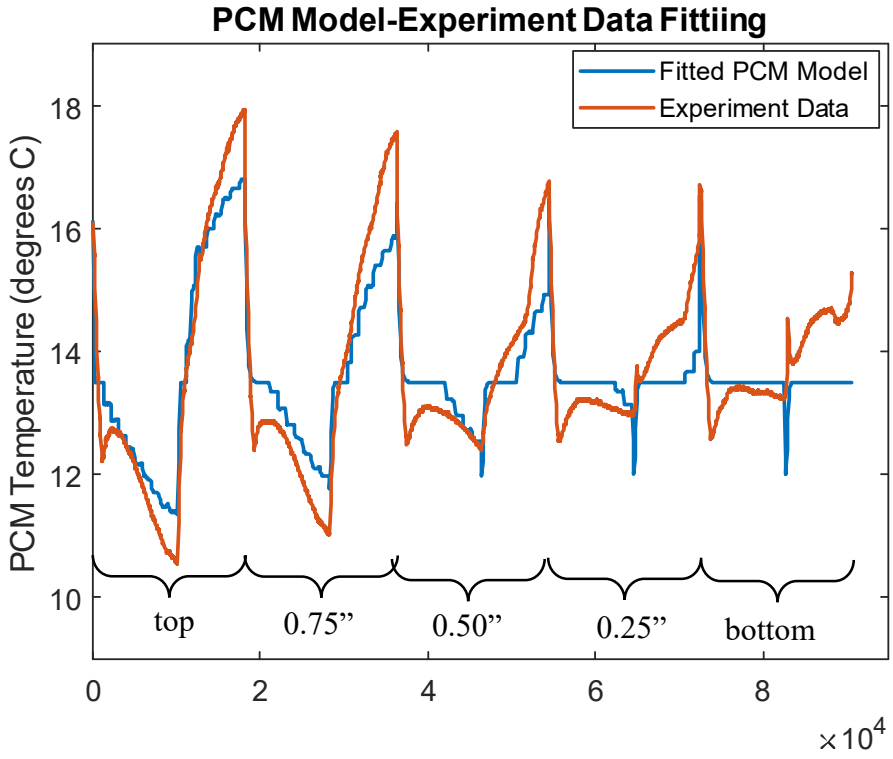

Figure 3.12. PCM Temperature predicted by the PCM model after the factor z is applied

3.4 EnergyPlus and Simulink Cosimulation Platform

3.4.1 Co-simulation Platform Description

The whole building energy simulation was performed using an EnergyPlus co-simulation platform in Simulink that was developed by my colleague, Aly Elhefny. The EnergyPlus Functional Mock-up Unit (FMU) file contains the building energy models and is linked to the PCM model using three primary interfacing variables, which are updated at each timestep in a

ping-pong scheme. Figure 3.13 displays a schematic drawing of the co-simulation. The EnergyPlus FMU outputs the supply-air mass flow rate and supply air temperature, which are input to the PCM model which outputs the temperature at the outlet of the PCM section after the PCM model's heat transfer calculations have been performed. The EnergyPlus FMU then inputs this temperature as the air temperature being supplied to the individual zones.

The building type used in the co-simulation was the three-floor prototypical medium office building, which contains 15 conditioned zones (3 core zones and 12 perimeter zones). Each floor has a dedicated air handling unit and a direct-expansion air-conditioning system. Each zone has a variable air volume terminal with reheat.

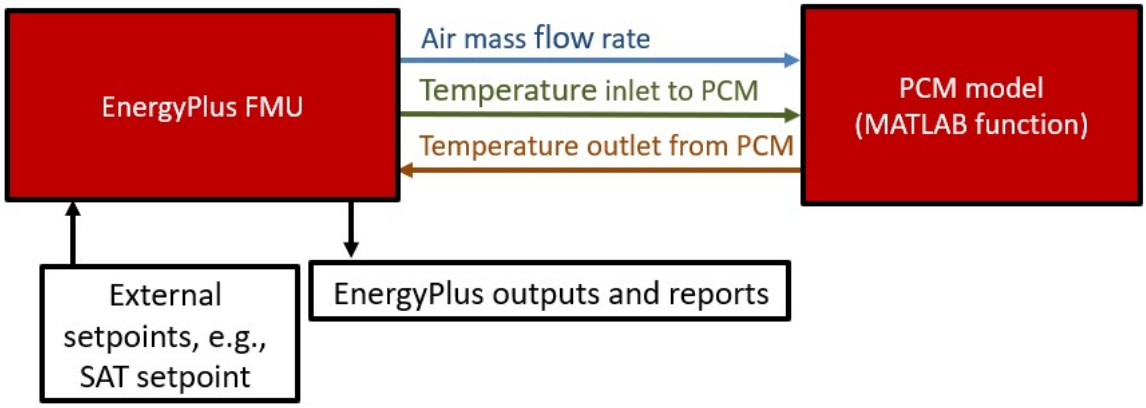

Figure 3.13. Schematic diagram of EnergyPlus co-simulation platform in Simulink developed by Aly Elhefny

3.4.2 Candidate Cities

The building loads and HVAC performance are dependent on the climate region that the building is located in. The whole building simulation was conducted for multiple cities to understand how the performance of the proposed PCM storage is affected by the climate location. Table 3.3 and Figure 3.14 display the candidate cities in which the whole building simulation was

conducted. The climate zones 1A, 3B and 5A are designated as hot-humid, hot-dry and cold, respectively. The U.S. Department of Energy (DOE) [36] defines the climate zones as follows:

1. Hot-humid

A hot-humid climate is generally defined as a region that receives more than 20 in. (50 cm) of annual precipitation and where one or both of the following occur:

- A 67°F (19.5°C) or higher wet bulb temperature for 3,000 or more hours during the warmest 6 consecutive months of the year; or
- A 73°F (23°C) or higher wet bulb temperature for 1,500 or more hours during the warmest 6 consecutive months of the year.

2. Hot-dry

A hot-dry climate is generally defined as a region that receives less than 20 in. (50 cm) of annual precipitation and where the monthly average outdoor temperature remains above 45°F (7°C) throughout the year.

3. Cold

A cold climate is generally defined as a region with approximately 5,400 heating degree days (65°F basis) or more and fewer than approximately 9,000 heating degree days (65°F basis).

These climate zones were chosen because they cover three opposing climates: the hot-humid climate will provide high external heat gains and high external latent load, the hot-dry climate will provide high external heat gains and low external latent load, and the cold climate will provide lower external heat gains. The HVAC system was sized by EnergyPlus according to the design conditions for each city and corresponding climate zone.

Table 3.3. Whole Building Simulation Candidate Cities

Candidate City	Climate Zone
Miami, Florida	1A
El Paso, Texas	3B
Buffalo, New York	5A

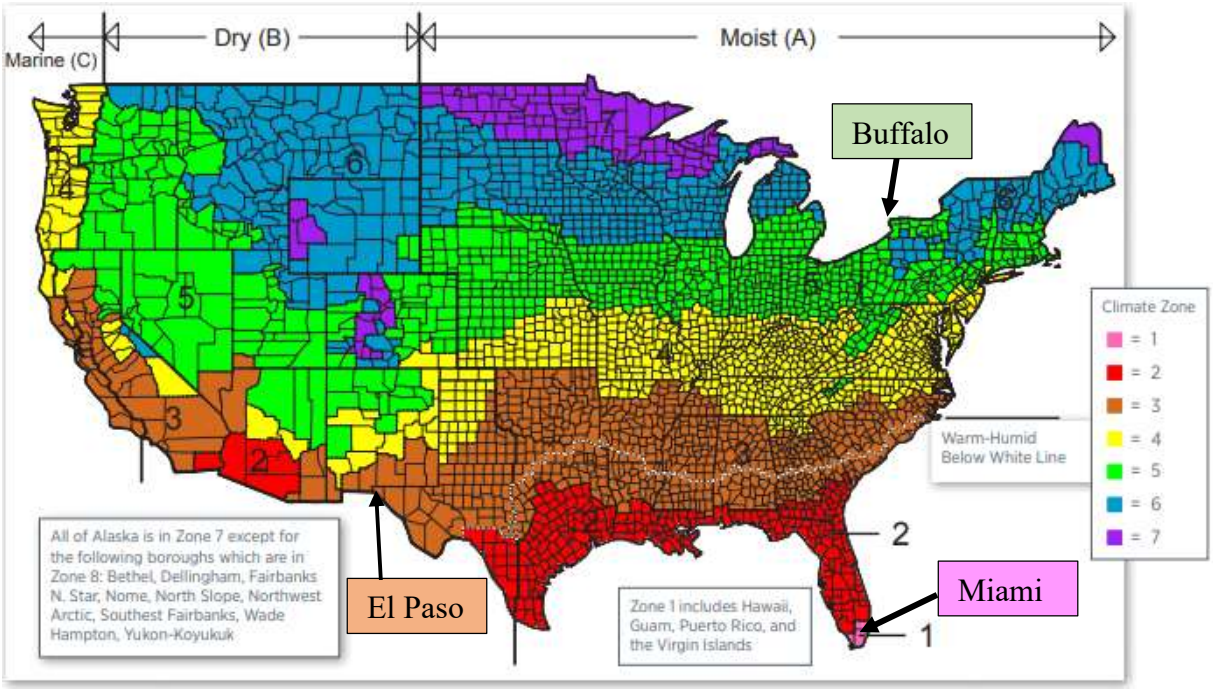

Figure 3.14. Location of candidate cities and ASHRAE climate zones [37]

3.5 Simulation Case Description

The whole building simulations consist of two cases: baseline and PCM-equipped. The baseline case is the case that simulates normal HVAC operation without the PCM in the duct and the SAT setpoint is set at a constant value of 12.7 °C. In this case, there is no interaction between the EnergyPlus FMU and the PCM model. The PCM-equipped case involves lowering the SAT setpoint to 9.2 °C from 6 AM to 12 PM (PCM charging period) and raising the SAT setpoint to

15.2 °C from 12 PM to 3 PM and 15.7 °C from 3 PM to 6 PM. The period from 12 PM to 6 PM (PCM discharging period) corresponds with the on-peak energy hours. The simulations were conducted for a 3-month cooling season from the beginning of June to the end of August.

For each case, the timestep in the EnergyPlus simulation is ten minutes. To ensure convergence requirements for the Enthalpy method are met, the timestep in PCM model is 0.5 s, which is implemented inside the MATLAB function block in Simulink.

3.6 PCM and Duct Sizing

The PCM mass was sized for each floor of the medium office building according to the on-peak HVAC sensible cooling energy usage for the hottest day of the whole cooling season. The baseline case was simulated for the 3-month cooling season and the day with the highest on-peak total HVAC sensible cooling energy (Q_s) was used as the design day. The PCM was sized to have total latent heat energy equal to one tenth of the maximum one-day on-peak HVAC sensible cooling energy:

$$m_{PCM} = \frac{Q_{s,max\ on-peak}}{10\ h_{sl}} \tag{3.22}$$

The duct in each floor was sized according to the maximum design airflow rate ($\dot{\forall}_{max}$) determined by EnergyPlus. The square duct width (W_d) was determined as

$$W_d = \sqrt{\frac{\dot{\forall}_{max}}{v_{max}}} \tag{3.23}$$

where v_{max} is the maximum recommended air velocity in a duct (1200 fpm). The duct wall thickness is set at 1.31 mm, which corresponds with 16-gauge galvanized steel. The total length

of the PCM duct section was 20 m and it was divided into 20 lengthwise subsections. The PCM thickness was determined using the PCM mass, total duct length and duct width.

4. Simulation Results

This section presents the results of the whole building simulation and the analysis to deduce meaningful insights on the load shifting capabilities of the PCM thermal energy storage. First, one day results for hot-dry and mild-humid days are presented and analyzed for El Paso. These two days were chosen because they have weather conditions that have high sensible and latent cooling loads, which will give insight into how these loads are shifted and their effect on the peak energy demand reduction. Then, the 3-month cooling season loads and energy costs are presented for each location. Lastly, the payback period for each location is determined.

4.1 PCM Charging/Discharging Rate

Figure 4.1 displays the supply-air temperature and post-PCM air temperature for each floor on a hot and dry day. The yellow shaded area represents the PCM charging period, and the green shaded area represents the PCM discharging period. During the charging process, the air temperature at the PCM section outlet is higher than the supply-air temperature, which is due to the heat gained by the air from the PCM. During the discharging process, the air temperature at the PCM section outlet is lower than the supply-air temperature, which is due to the heat lost by the air to the PCM. Figure 4.2 displays the air-to-PCM heat transfer rate profile for each floor on a hot and dry day, which is the rate that the PCM loses (positive) and gains (negative) thermal energy in the charging and discharging periods, respectively. Figure 4.3 displays the latent heat ratio (LHR), which signifies how much of the PCM has melted or frozen and how much of the PCM's latent heat capacity is utilized during the charging and discharging process. The LHR is the mean value of the ratio between the enthalpy and h_{sl} for all the PCM nodes. When the averaged enthalpy is greater than h_{sl}, LHR is 1, and when the enthalpy is less than h_{sl}, LHR is 0. The PCM

begins in a liquid phase with the LHR equal to 1. The LHR dropped to below 0.1 during the charging process, which means that more than 90 % of the PCM's latent storage capacity is used. The supply air temperature increases above the PCM's melting temperature in the discharging process, which causes the LHR to increase to above 0.95.

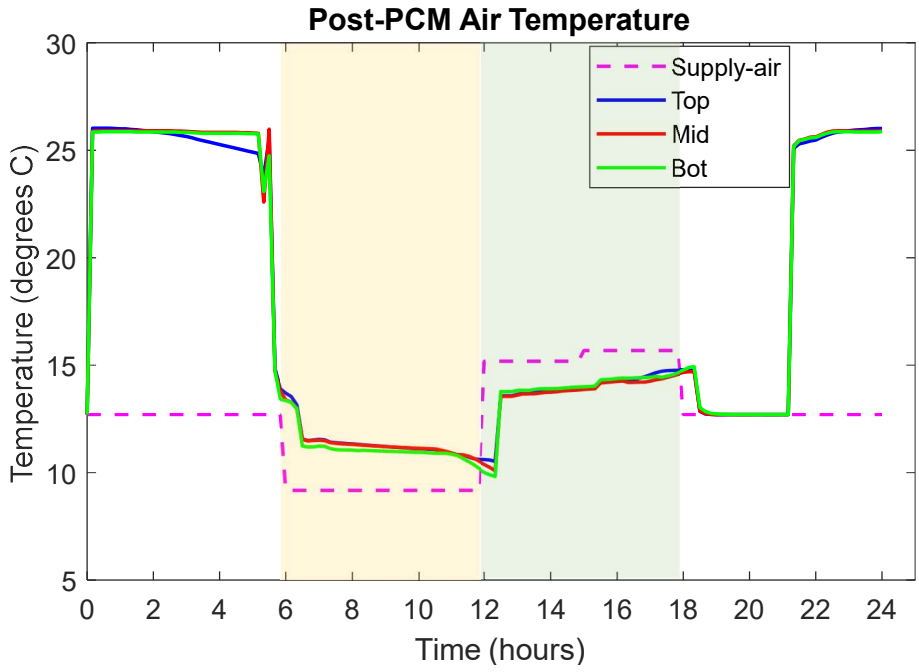

Figure 4.1. Post-PCM air temperature profile on a hot-dry day

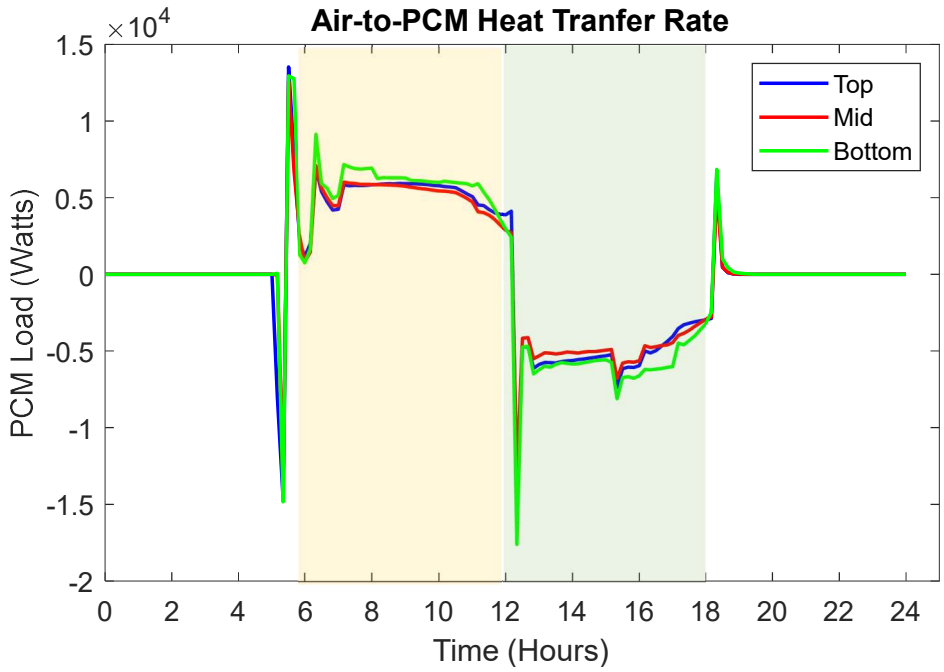

Figure 4.2. Air-to-PCM heat transfer rate profile for each floor during a hot and dry day

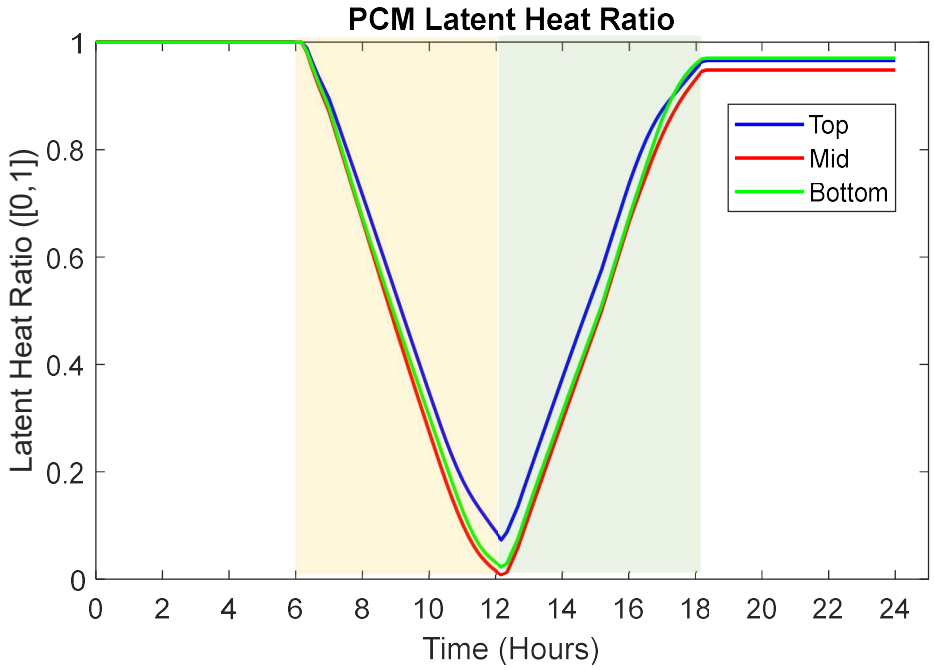

Figure 4.3. Latent heat ratio profile for each floor during a hot and dry day

4.2 HVAC Sensible Cooling Load

Figure 4.4 displays the total HVAC sensible cooling load profile for the baseline and PCM-equipped cases on hot-dry and mild-humid days. The addition of the PCM results in an increase in the HVAC sensible load during the charging period due to the lower supply-air temperature and a decrease during the discharging period due to the lower supply-air temperature. The amount of the load that is shifted from the on-peak hours to the off-peak hours on the hot-dry day is 389 MJ, which equates to 11.4 % of the baseline on-peak sensible load. The amount of the load that is shifted from the on-peak hours to the off-peak hours on the mild-humid day is 306 MJ, which equates to 14.9 % of the baseline on-peak sensible load.

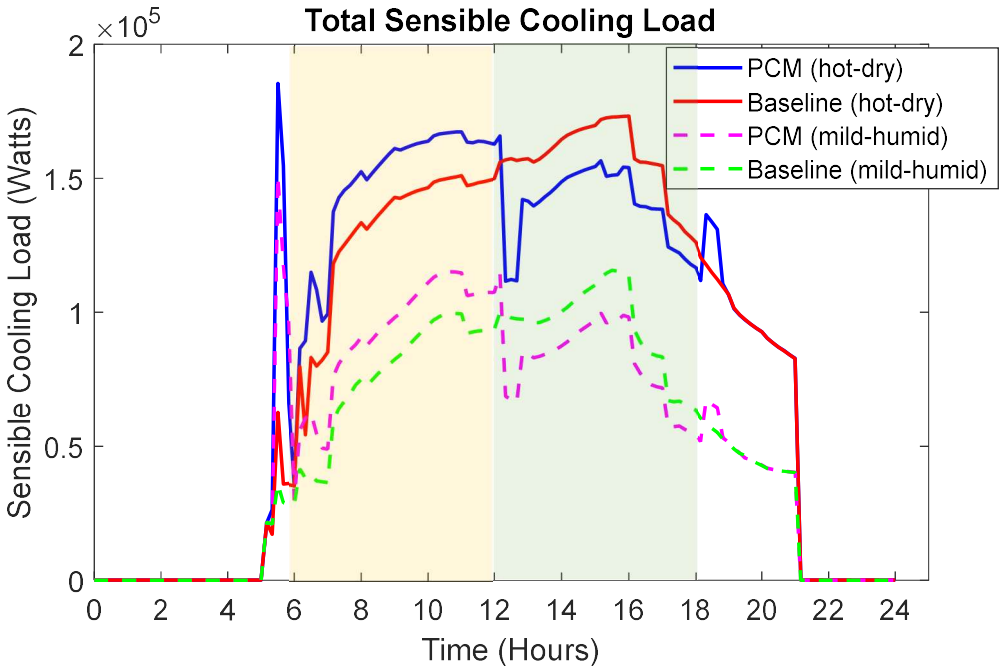

Figure 4.4. Total HVAC sensible load profile for a hot-dry day and a mild-humid day

4.3 HVAC Latent Cooling Coil Load

Figure 4.5 displays the HVAC latent cooling load profile for the baseline and PCM-equipped cases on hot-dry and mild-humid days. The addition of the PCM results in an increase in the HVAC latent cooling load during the charging period and a decrease during the discharging period. The load is higher during the charging period in the PCM-equipped case because the supply air temperature is lower, which leads to a lower evaporating temperature and more removal of water vapor from the air. Conversely, the supply air temperature is higher in the discharging period, which results in less dehumidification because of the higher evaporating temperature and lower moisture level in the re-circulating air. This effect is not attributed to the presence of the PCM, but the variation of the supply-air temperature during the charging and discharging periods. Figure 4.17 displays a core zone's relative humidity profile for the baseline and PCM-equipped cases on a mild and humid day. During the PCM charging period, the relative humidity is lower for the PCM-equipped case than the baseline case because of the additional dehumidification of the supply air. During the PCM discharging period, relative humidity is higher for the PCM-equipped case than the baseline case because there is less dehumidification of the supply air due to the higher supply air temperature. The amount of the latent load that is shifted from the on-peak hours to the off-peak hours on the hot-dry day is 25.7 MJ, which equates to 52.9 % of the baseline on-peak latent load. The amount of the latent load that is shifted from the on-peak hours to the off-peak hours on the mild-humid day is 279 MJ, which equates to 40.2% of the baseline on-peak latent load. The mild-humid day has a higher latent cooling load than the hot-dry day due to the higher moisture content of the air in the outdoor environment.

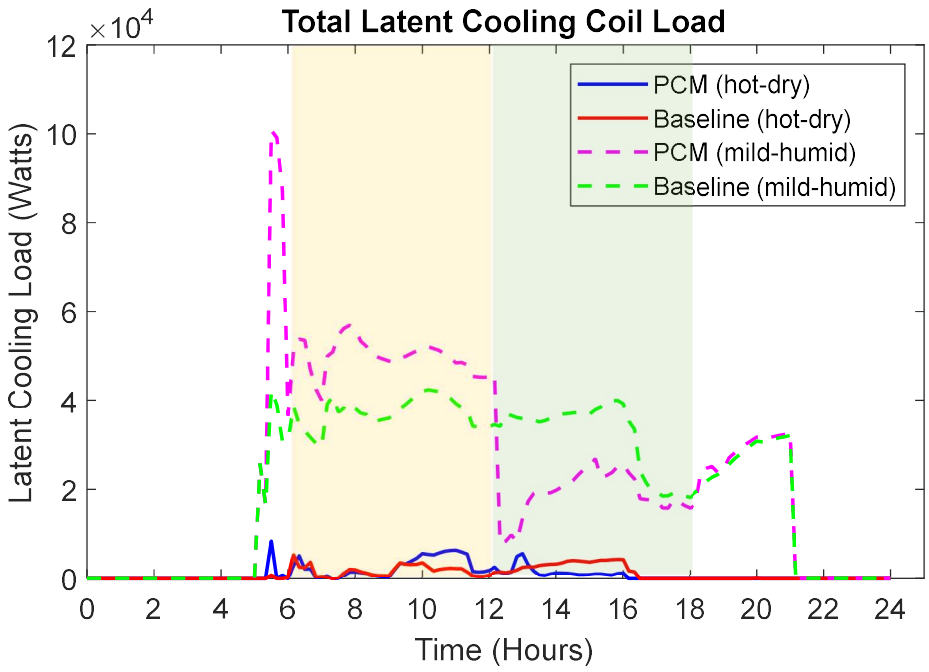

Figure 4.5. Total HVAC latent load profile for a hot-dry day and a mild-humid day

4.4 Total HVAC Cooling Load

Figure 4.6 and Figure 4.7 display the total HVAC cooling load profile for the baseline and PCM-equipped cases on hot-dry and mild-humid days. The amount of the load that is shifted from the on-peak hours to the off-peak hours on the hot-dry day is 414 MJ, which equates to 12.0 % of the baseline on-peak total cooling load. The amount of the load that is shifted from the on-peak hours to the off-peak hours on the mild-humid day is 586 MJ, which equates to 21.3 % of the baseline on-peak total cooling load. The amount of load shifted is higher for the mild-humid day than the hot-dry because of the higher latent cooling load shifted during the mild-humid day.

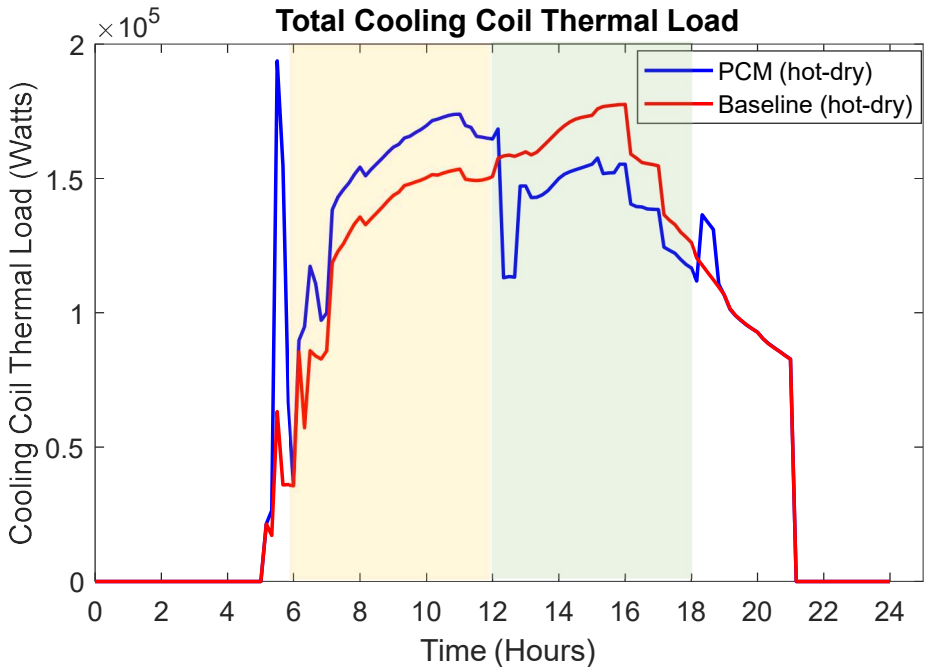

Figure 4.6.Total HVAC load profile for a hot-dry day

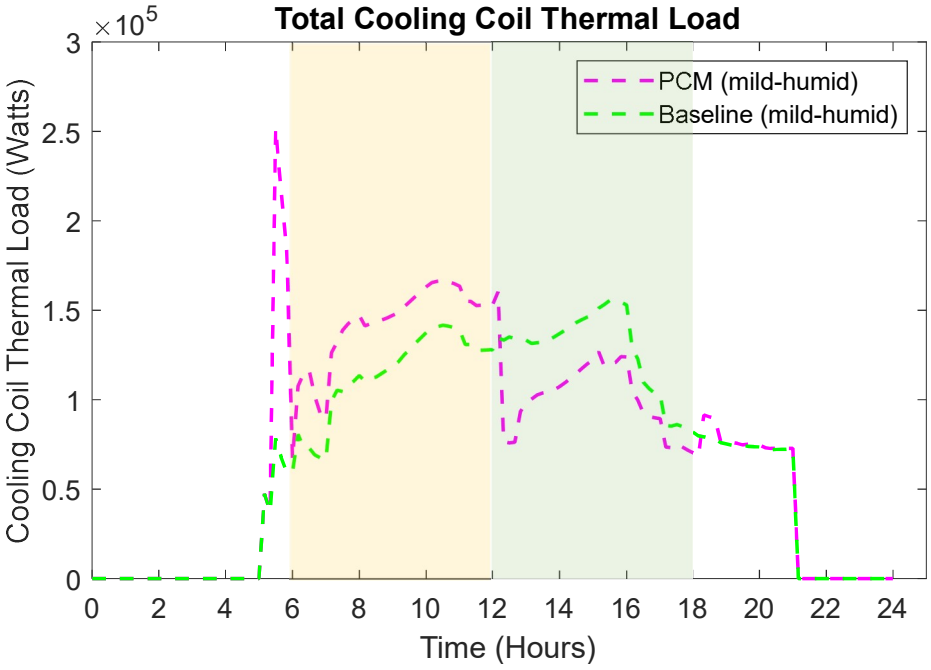

Figure 4.7. Total HVAC load profile for a mild-humid day

4.5 Total Cooling Coil Power

Figure 4.8 displays the total HVAC cooling coil electric power consumption (compressor and condenser fan power) profile for the baseline and PCM-equipped cases on hot-dry and mild-humid days. The amount of the compressor power usage that is shifted from the on-peak hours to the off-peak hours on the hot-dry day is 56.2 kWh, which equates to 22.6 % of the baseline on-peak electric load. The amount of the electric load that is shifted from the on-peak hours to the off-peak hours on the mild-humid day is 34.4kWh, which equates to 29.9 % of the baseline on-peak electric load. The percentage of the electric load shifted is higher than the corresponding thermal load shift due to the higher compressor COP during on-peak hours, which the ratio between the total cooling load and the total cooling coil electric power, for the PCM-equipped case. Figure 4.9 displays the compressor COP profile for the baseline and PCM-equipped cases on hot-dry and mild-humid days. In both days, the compressor COP was higher for the PCM-equipped case during the PCM discharging. This is because a higher SAT would increase the COP with a reduced pressure lift across the compressor, so the compressor will require less work input to provide the same amount of cooling.

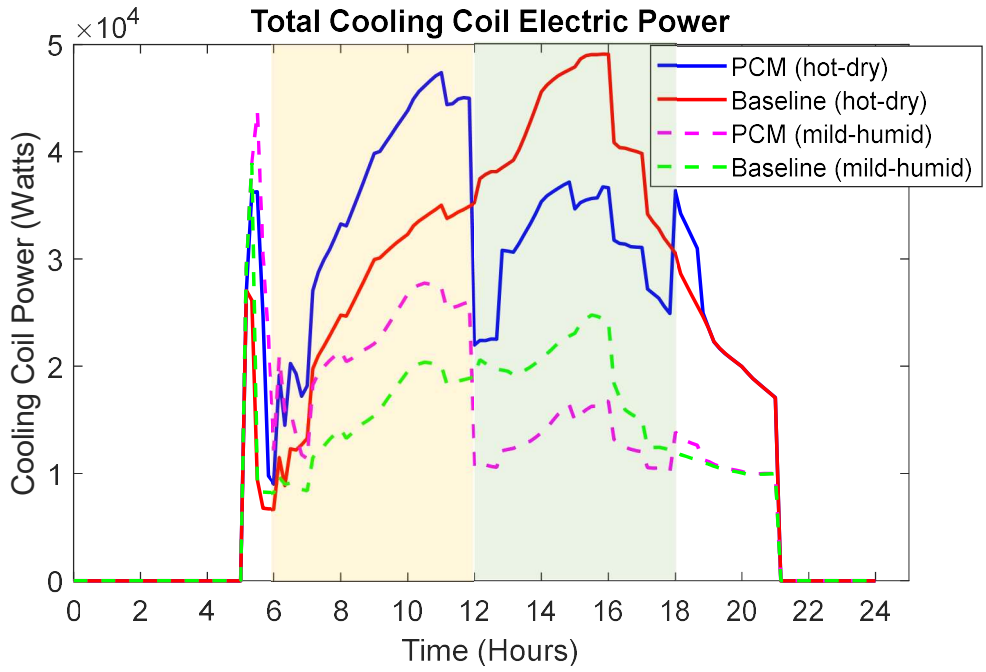

Figure 4.8. Total cooling coil electric power profile for a hot-dry day and a mild-humid day

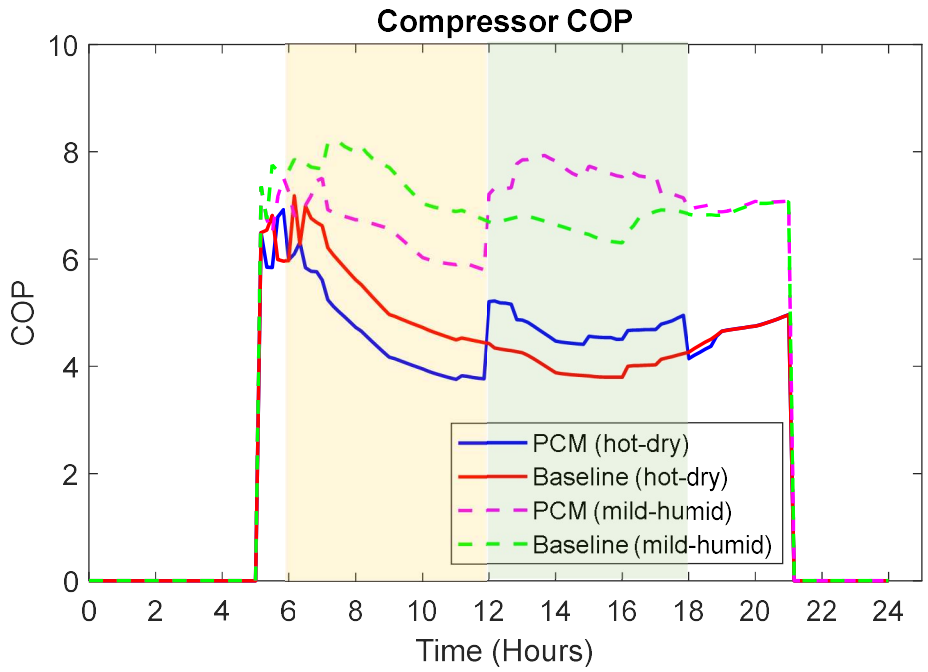

Figure 4.9. Compressor COP profile for a hot-dry day and a mild-humid day

4.6 Total Fan Power

Figure 4.10 displays the total fan electric power consumption profile for the baseline and PCM-equipped cases on a hot-dry day. The amount of on-peak fan electric load increases by 8.27 kWh, which equates to a 35.9 % increase. It may be noted that the fan power represents a small fraction of the total HVAC power use and the increase in the on-peak fan power usage can be well compensated for by the compressor power reduction, which will be discussed in the next subsection. Since the supply air temperature is decreased in the charging period, a lower air mass flow rate is required to provide cooling to the building zones. The mass flow rate increases during the discharging period because the supply air temperature is increased, and more air is required to provide sufficient cooling. The total air mass flow rate profile for the baseline and PCM cases on a hot-dry day is displayed in Figure 4.11.

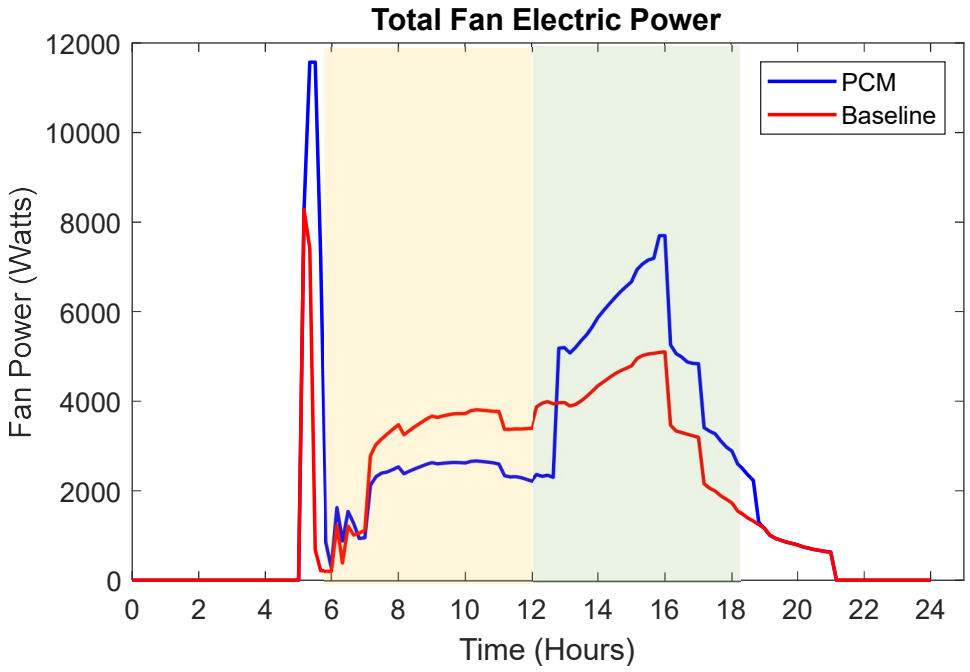

Figure 4.10. Total fan electric power profile for a hot-dry day

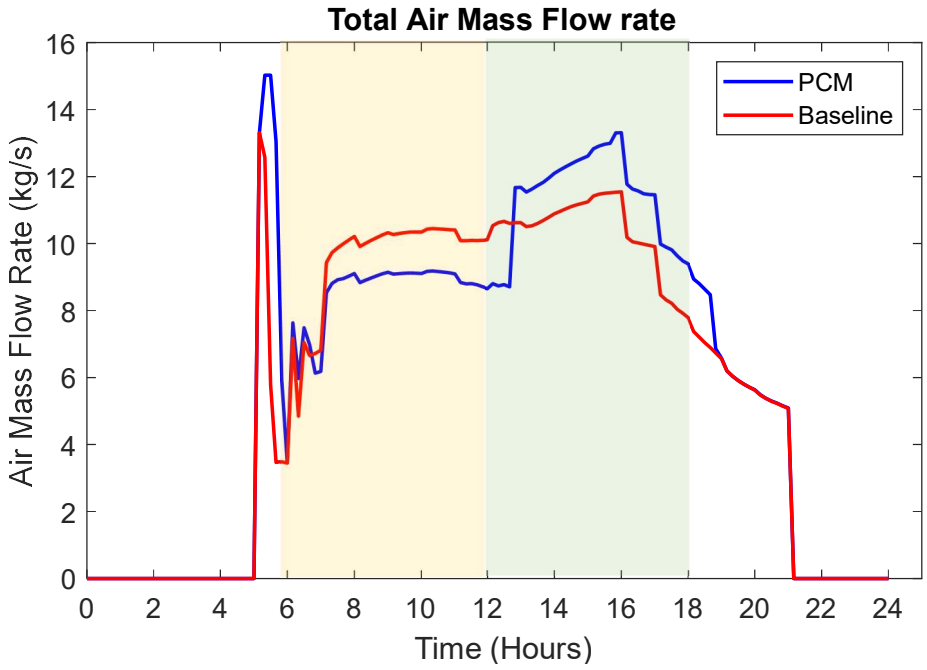

Figure 4.11. Total air mass flow rate profile for a hot-dry day

4.7 Total HVAC Power Reduction

Figure 4.12 displays the total HVAC electric power consumption profile for the baseline and PCM-equipped cases on hot-dry and mild-humid days. Although the fan power is increased during the on-peak hours, the compressor power reduction is dominant leading to much reduced on-peak HVAC electricity usage. The amount of the electric load that is shifted from the on-peak hours to the off-peak hours on the hot-dry day is 47.9 kWh, which equates to 17.6 % of the baseline on-peak electric load. The on-peak peak demand of the HVAC electric power on the hot-dry day was reduced by 9.65 kW, which equates to a reduction by 17.8 %. The amount of the electric load that is shifted from the on-peak hours to the off-peak hours on the mild-humid day is 31.9 kWh, which equates to 25.3 % of the baseline on-peak total electric load. The on-peak peak demand of the HVAC electric power on the mild-humid day was reduced by 6.63 kW, which equates to a reduction by 24.0 %. Figure 4.13 displays the system COP for the baseline and PCM-equipped

cases on hot-dry and mild-humid days, which is defined as the ratio between the total cooling load and the total HVAC electric power. For both days the system COP is higher during the PCM discharging period for the PCM equipped case, which means that less work input is required to provide the same amount of cooling. This leads to a further reduction of the on-peak power consumption that is primarily driven by the thermal load shifting.

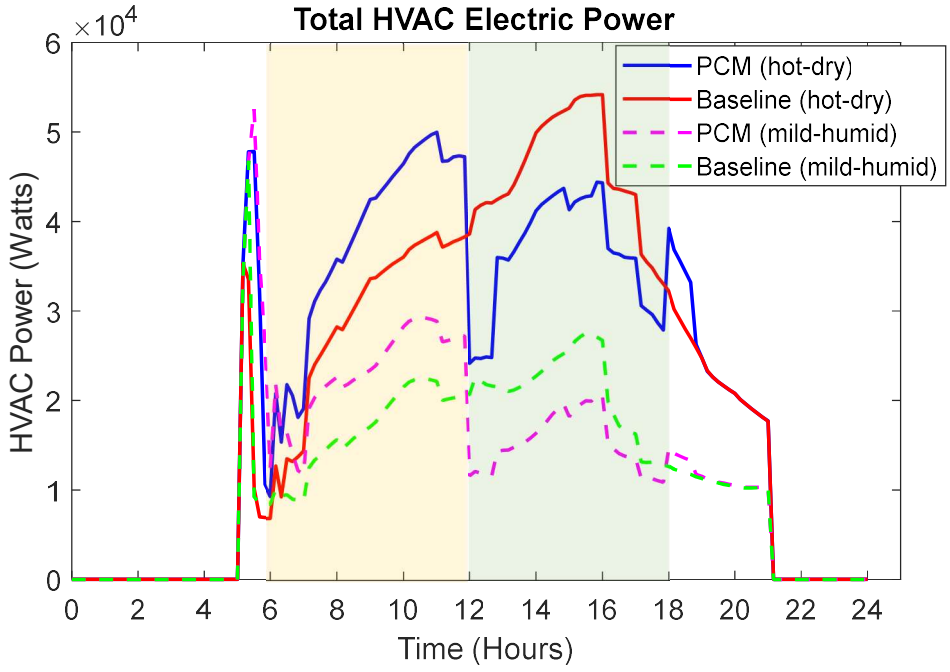

Figure 4.12. Total HVAC electric power profile for a hot-dry day and a mild-humid day

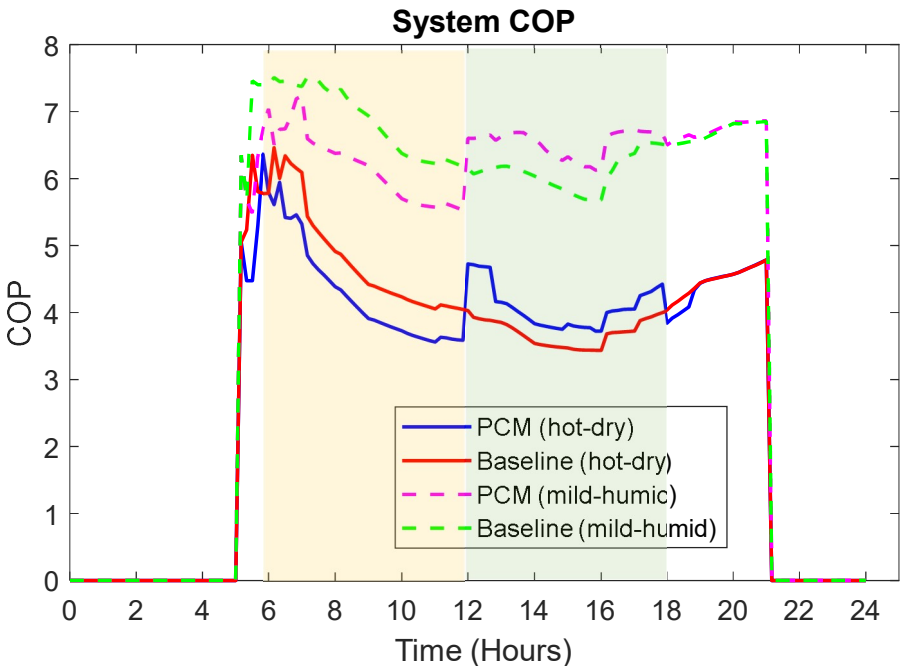

Figure 4.13. System COP profile for a hot-dry day and a mild-humid day

4.8 Zone Temperature and Relative Humidity

Figure 4.14 and Figure 4.15 display the variation of the dry-bulb air temperature in a core zone, perimeter zone and outdoor environment for the baseline and PCM-equipped cases on hot-dry and mild-humid days, respectively. The zone temperature was maintained at 24 °C during the occupied hours, which ensured that the occupants were experiencing a comfortable temperature despite the addition of the PCM. Figure 4.16 and Figure 4.17 display the variation of the relative humidity in a core zone and outdoor environment for the baseline and PCM-equipped cases on hot-dry and mild-humid days, respectively. The comfort range for the zone relative humidity is 0.25 to 0.6 and is represented by the blue-shaded are in the figures. In both days, the zone relative humidity was maintained in the comfort zone during the occupied hours. Since there was little latent load shifting for the hot-dry day, the relative humidity profile is similar for the baseline and PCM-equipped cases. On the other hand, during the mild-humid day the relative humidity for the

PCM-equipped case was lower in the PCM charging period than the baseline case. This is due to the increased dehumidification caused by lowering the SAT. The relative humidity was higher in the PCM discharging period because the SAT was increased, which led to less dehumidification of the supply air.

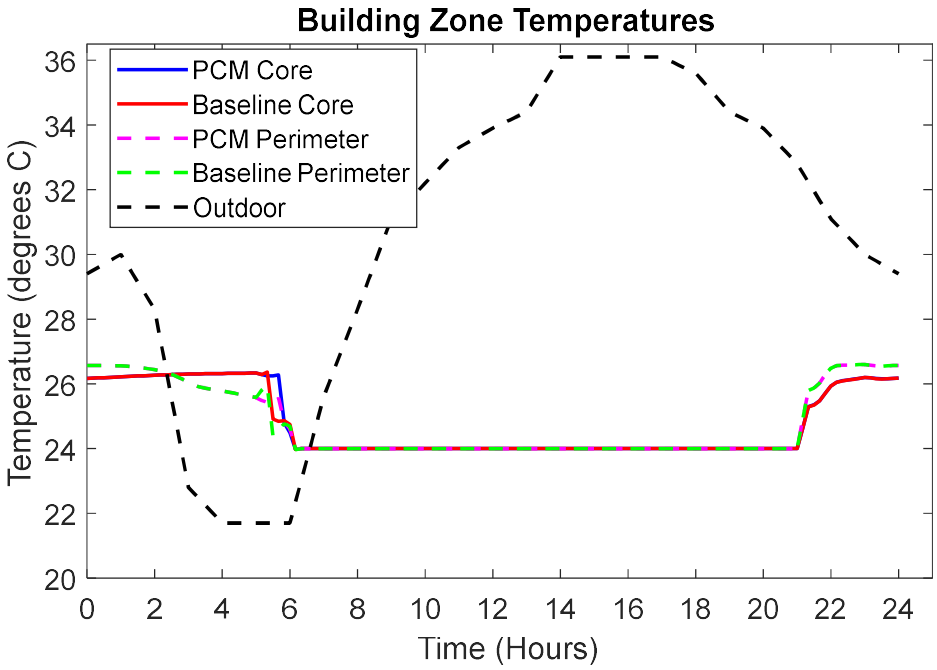

Figure 4.14. Zone temperature profile for a hot-dry day

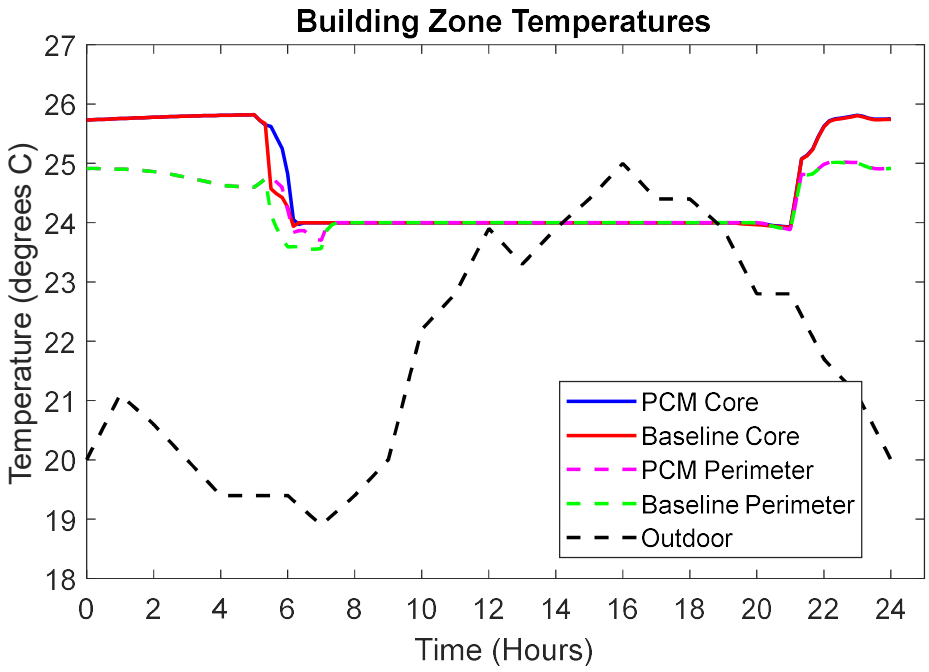

Figure 4.15. Zone temperature profile for a mild-humid day

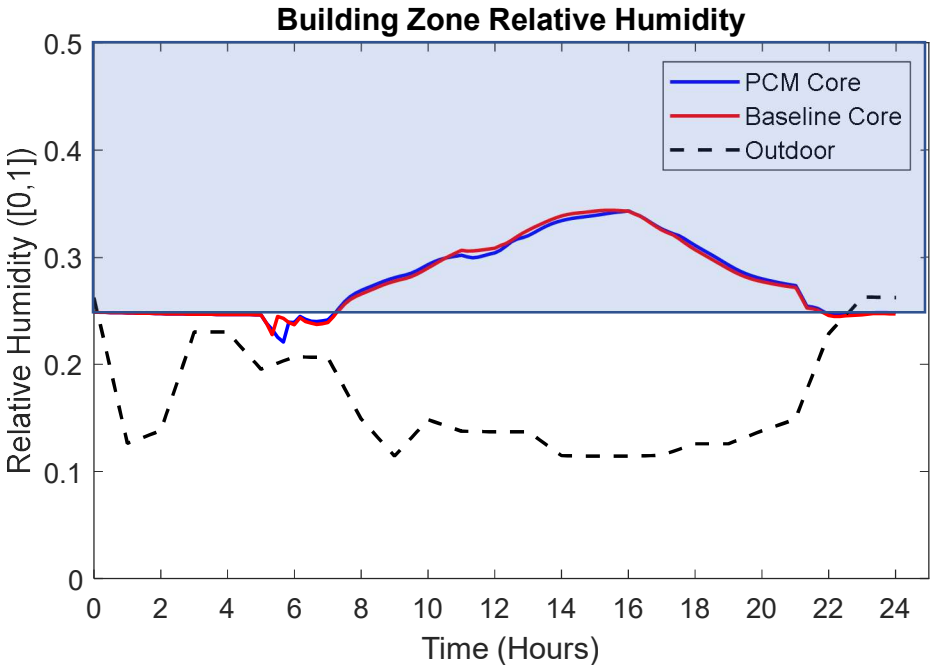

Figure 4.16. Zone relative humidity profile for a hot-dry day

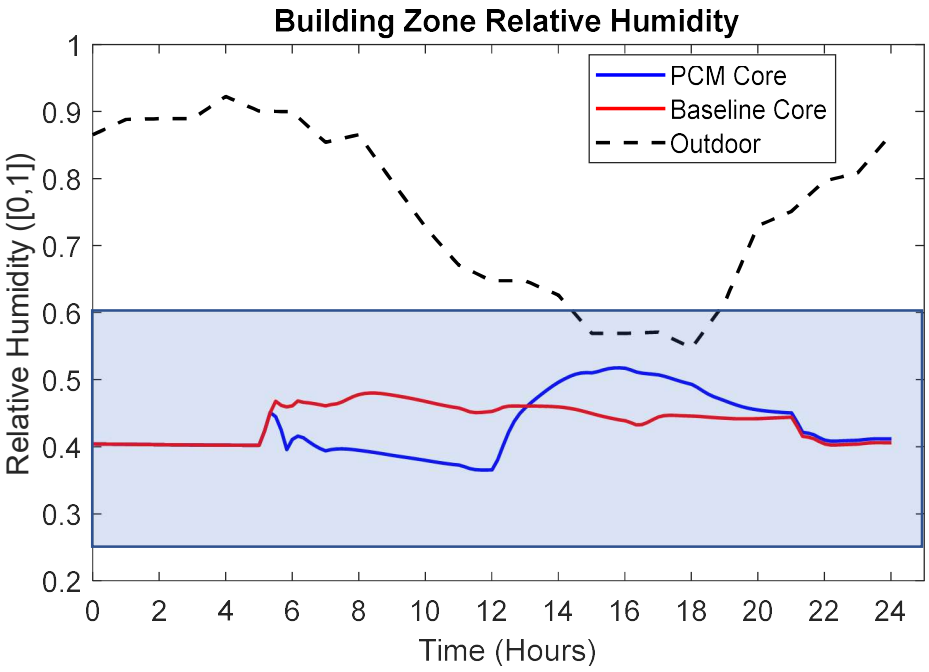

Figure 4.17. Zone relative humidity profile for a mild-humid day

4.9 Indoor Air Quality Requirements

ASHRAE 90.1 imposes a minimum zone airflow rate of 30% of the zone peak airflow rate to provide sufficient ventilation to the zone and maintain indoor air quality standards [38]. Figure 4.18 and Figure 4.19 display the zone airflow rate and airflow ratio profile for a perimeter zone on a mild-humid day in El Paso. The zone airflow ratio is the ratio between the zone airflow rate and the peak zone airflow rate. EnergyPlus reported the peak zone airflow rate to be 0.649 m^3/s for this specific zone. The PCM case led to a decrease in the zone airflow rate during the charging period because of the decrease in the supply air temperature. Despite the decrease in zone airflow rate, the airflow ratio is above 0.3 during the occupied hours from 8AM to 6PM, which satisfies the requirements of ASHRAE 90.1. Therefore, the implementation of PCM TES does not lead to poor indoor air quality. Since the zone airflow rate is higher in hotter days to provide sufficient cooling for the higher loads, the ratio will be higher than 0.3 for those days as well.

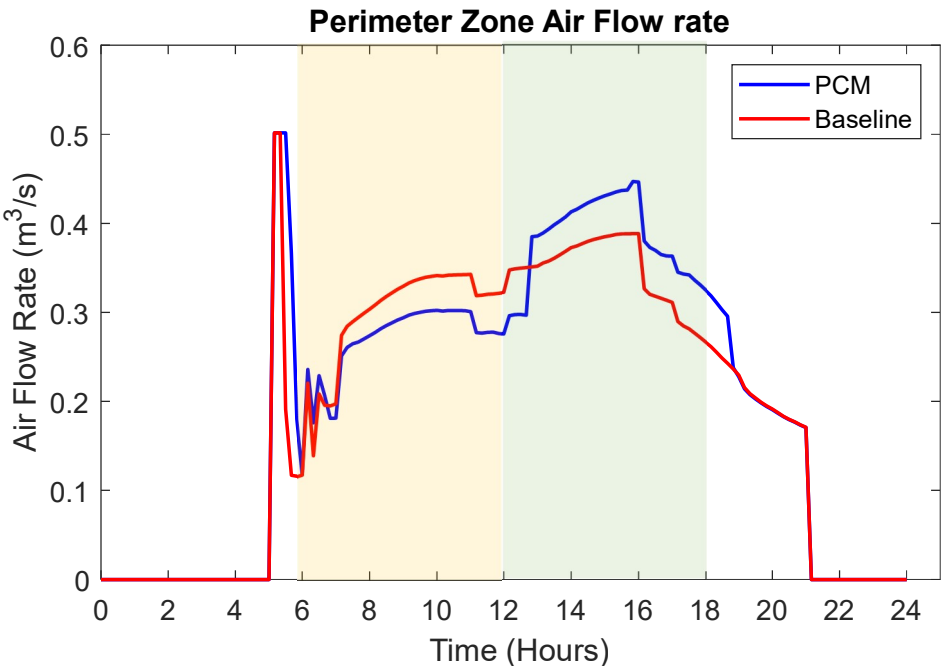

Figure 4.18. Perimeter zone airflow rate profile for a mild-humid day

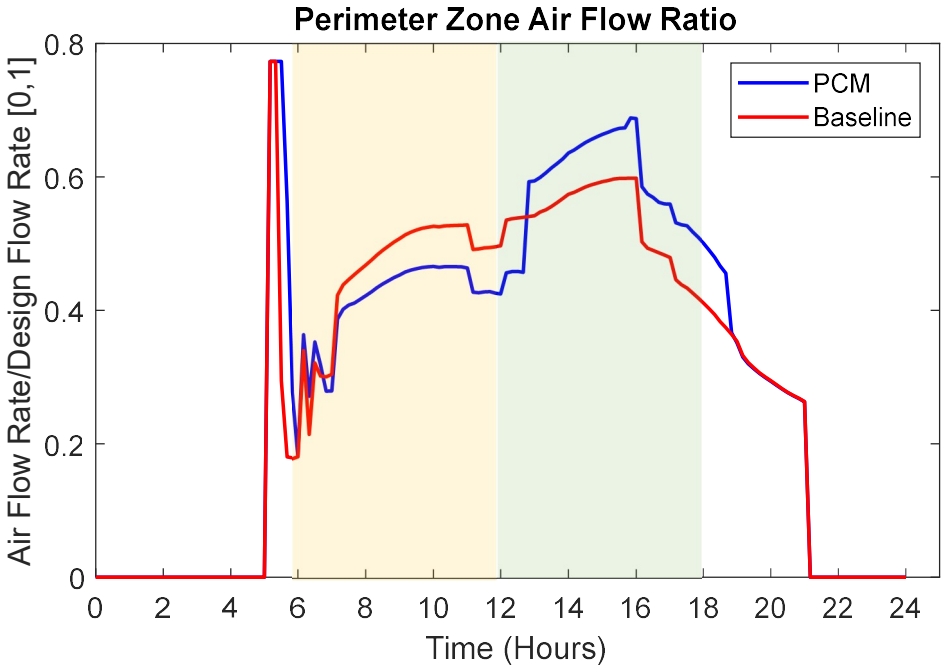

Figure 4.19. Perimeter zone airflow ratio profile for a mild-humid day

4.10 Total HVAC Energy Cost

4.10.1 Electricity Rate Schedules

The total HVAC energy cost was calculated using the TOU electricity rates charged by energy providers in the three locations. The rates used in the cost calculation correspond to the summer months. Table 4.1 displays a breakdown of the utility rates. The rates comprise two charges: the energy charge and the demand charge. The energy charge is the cost of the electrical energy ($/kWh) and is calculated at each timestep according to the specific rate at that time. The demand charge is the cost of providing the highest electrical demand, in kW, over a 30-minute interval in a month and is calculated at the end of each month.

Table 4.1. Summer energy and demand rates for the three locations

City	Rate name	Energy rate ($/kWh)			Demand Charge ($/kW)	
		On-Peak	Mid-peak	Off-peak	On-peak	Anytime
El Paso	EL PASO ELECTRIC COMPANY SCHEDULE NO. 24 [39]	0.11861 (12-6PM)	—	0.00502 (12AM-12PM and 6PM-12AM)	—	24.50
Miami	Florida Power & Light Company General Service Demand-TOU (GSDT-1) [40]	0.07078 (12-9PM)	—	0.03272 (12AM-12PM and 9PM-12AM)	9.98	—
Buffalo	Orange and Rockland Utilities Time of Use [41]	0.32012 (12-7PM)	0.1145 (10AM-12PM and 7-9PM)	0.02061 (12AM-10AM and 9PM-12AM)	—	—

4.10.2 Electricity Cost

The total on-peak HVAC electricity consumption and HVAC electricity cost are displayed in Figure 4.20 and Figure 4.21 for the baseline and PCM-equipped cases in El Paso, Miami and Buffalo over the duration of the 3-month cooling season. The total on-peak electric consumption was decreased by 4074 kWh (25.0%) in El Paso, 4511 kWh (20.0%) in Miami and 3349 kWh (23.4%) in Buffalo. Miami had the highest on-peak electricity consumption due to the hot and humid climate, which leads to high sensible and latent cooling loads. As a result, there was a higher amount of load shifting that took place. The total electricity cost was decreased by $889.00 (12.3%) in El Paso, $472.00 (9.6%) in Miami and $812.00 (14.5%) in Buffalo. Despite having the highest total decrease in on-peak electricity consumption, Miami had the lowest electricity cost saving because it had the least aggressive rate scheduling. The on-peak energy charge is 24x higher in El Paso, 2x higher in Miami and 16x higher in Buffalo than the off-peak charge. Therefore, the rate schedule in Miami does not incentivize load shifting as much compared to El Paso and Buffalo.

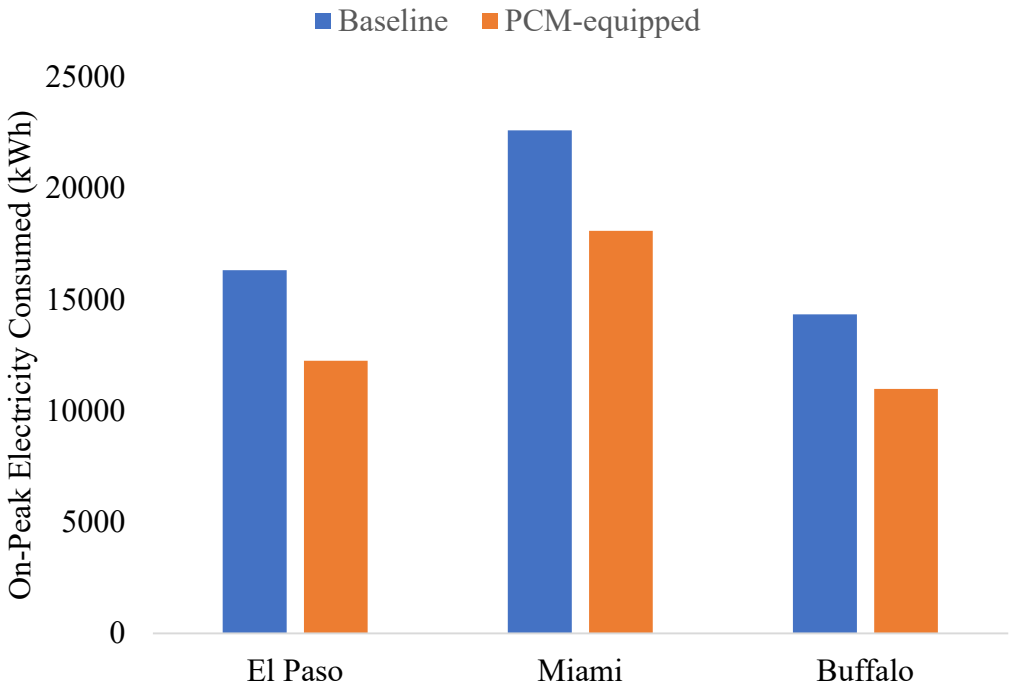

Figure 4.20. Total on-peak electricity consumed by HVAC system for the baseline and PCM-equipped cases in various cities

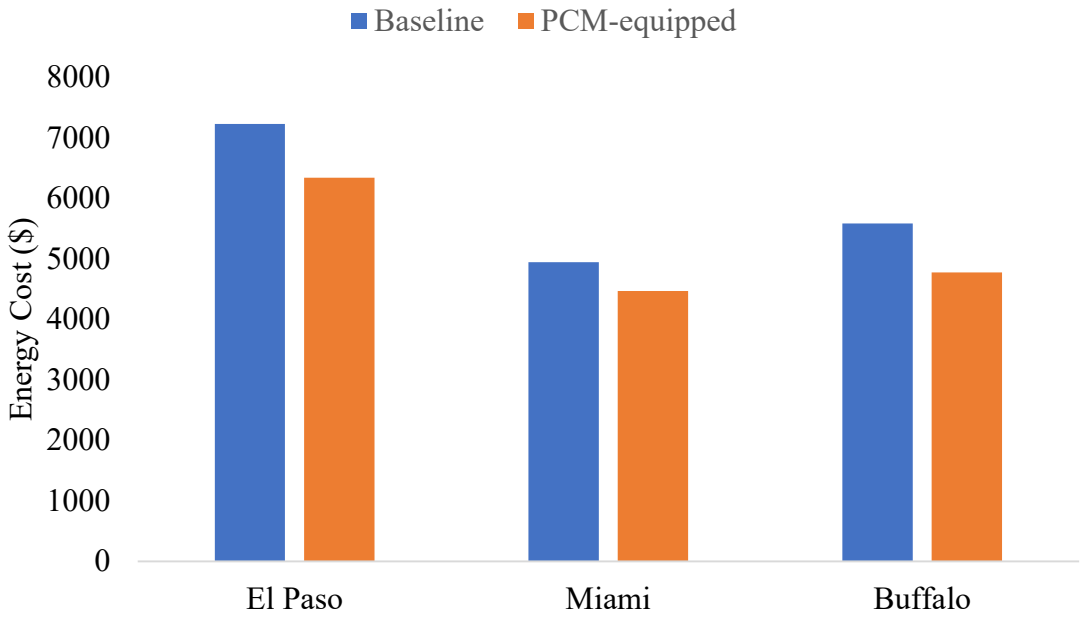

Figure 4.21. Total energy cost contributed by HVAC system for the baseline and PCM-equipped cases in various cities

4.11 Cooling Season Energy and Cost Summary

Table 4.2, Table 4.3 and Table 4.4 display the total loads, electric energy and electricity cost for the whole simulation period in El Paso, Miami and Buffalo, respectively. Miami had the highest total cooling load due to high sensible and latent load, which is characteristic of the hot-humid climate. This climate has the highest potential for load shifting because the implementation of the PCM TES will shift both the sensible and the latent load. For all cities, the average system COP is slightly lower in the PCM-equipped case than the baseline case. This is because the increase in the COP during the PCM discharging period is smaller than the decrease during the PCM charging period, as shown in Figure 4.13. Despite using more electric energy overall, the electricity cost is lower in

all cities because the consumption was shifted from the on-peak hours to the off-hours, leveraging the use of cheaper electricity during off-peak hours.

Table 4.2. El Paso - Cooling season total energy and electricity cost

	Baseline	PCM-equipped
Cooling Coil Sensible Load (GJ)	490	518
Cooling Coil Latent Load (GJ)	117	125
Cooling Coil Total Load (GJ)	607	643
Cooling Coil Electric Energy (MWh)	35.7	37.8
Supply Fan Electric Energy (MWh)	3.0	3.7
Total Electric Energy (MWh)	38.7	41.5
System COP	4.4	4.3
Total PCM (kg)	—	1915
Total Electricity Cost ($)	7227	6338
On-Peak Electric Energy (kWh)	16325	12251

Table 4.3. Miami - Cooling season total energy and electricity cost

	Baseline	PCM-equipped
Cooling Coil Sensible Load (GJ)	488	521
Cooling Coil Latent Load (GJ)	392	403
Cooling Coil Total Load (GJ)	880	924
Cooling Coil Electric Energy (MWh)	51.2	55.2
Supply Fan Electric Energy (MWh)	3.1	3.6
Total Electric Energy (MWh)	54.3	58.8
System COP	4.5	4.4
Total PCM (kg)	—	2418
Total Electricity Cost ($)	4940	4468
On-Peak Electric Energy (kWh)	22602	18091

Table 4.4. Buffalo - Cooling season total energy and electricity cost

	Baseline	PCM-equipped
Cooling Coil Sensible Load (GJ)	411	436
Cooling Coil Latent Load (GJ)	228	236
Cooling Coil Total Load (GJ)	639	672
Cooling Coil Electric Energy (MWh)	31.9	34.3
Supply Fan Electric Energy (MWh)	2.4	2.9
Total Electric Energy (MWh)	34.3	37.2
System COP	5.2	5.0
Total PCM (kg)	—	1902
Total Electricity Cost ($)	5582	
On-Peak Electric Energy (kWh)	14332	10983

4.12 Payback Analysis

A simple payback analysis was performed to determine how long it would take to recover the cost of the PCM. The payback years were calculated as follows:

$$Payback\ years\ = \frac{Cost\ of\ PCM}{Annual\ Cooling\ Season\ Electricity\ Cost} \quad 4.24$$

The cost of the PCM was assumed to be $2 per kg [42]. The payback years for each city are displayed in Table 4.5. El Paso had the lowest payback period (4.3 years) among the cities. This was due to the high energy cost savings in El Paso and a relatively low total PCM cost. Buffalo had a slightly higher payback period (4.7 years) because it had lower energy cost savings and similar PCM cost. Since Miami used the most PCM and involved the lowest energy cost saving, it had the highest payback period (10.2 years).

Table 4.5. Payback years for PCM cost in the candidate cities

City	PCM Cost ($)	Payback years
El Paso	3830	4.3
Miami	4836	10.2
Buffalo	3804	4.7

5. Conclusion

In this thesis, the energy cost savings, on-peak load shifting, and peak electric demand reduction potentials were evaluated for a PCM based TES system designed for installations in supply-air duct. A numerical model for the PCM in the duct was formulated and calibrated using experimental data. The model was linked with EnergyPlus through FMU to perform whole building simulations for a medium office in three different climate regions over a 3-month cooling season. The PCM TES was able to shift the sensible HVAC load from the on-peak to off-peak hours due to the lowering of the SAT to store "cooling" energy in the PCM during the charging process and raising of the SAT to release the "cooling" energy in the PCM during the discharging process. Due to the lower SAT during the charging process, there was more dehumidification in the morning. On the other hand, there was less dehumidification during the afternoon hours when the SAT was raised. This led to a shift in the latent HVAC load from the on-peak to off-peak hours. The shift in the total cooling load resulted in a shift in the HVAC electric power consumption because less work input is required to provide cooling in the on-peak hours and more work input is required to provide the additional cooling in the off-peak hours. Miami had the highest on-peak load reduction because its hot-humid climate meant that it had a high sensible load, which led to a large PCM size, and high latent load. However, since it had the least aggressive price difference between on-peak and off-peak hours, it had the lowest electricity cost savings. El Paso had the most aggressive TOU rate schedule so it had the highest energy cost savings. Similarly, El Paso had the shortest payback period of 4.3 years. In actual building operations, the payback period is expected be shorter when the cost analysis is extended to other months where space cooling is still required; for commercial buildings whose cooling loads are mainly internal gain driven, space cooling is usually required throughout the whole year.

The work done in this thesis can be extended to gain a better understanding of the cost saving potential of PCM in the supply-air duct:

1. Full scale experiments can be conducted to validate the simulation results and determine the load shifting potential under real life conditions.
2. PCM thermal enhancement strategies can be investigated to improve the charge rate, and increase the load reduction potential.
3. A comprehensive bill of material and labor costs need to be determined to understand the actual capital investment and total payback period.

References

[1] B. Jones-Albertus, "Confronting the Duck Curve: How to Address Over-Generation of Solar Energy," Office of Energy Efficiency and Renewable Energy, 12 October 2017. [Online]. Available: https://www.energy.gov/eere/articles/confronting-duck-curve-how-address-over-generation-solar-energy. [Accessed 28 November 2020].

[2] US Department of Energy, "Energy Efficiency Trends in Residential and Commercial Buildings," 2010.

[3] M. Iten, S. Liu and A. Shukla, "A review on the air-PCM-TES application for free cooling and heating in the buildings," *Renewable and Sustainable Energy Reviews,* vol. 61, pp. 175-186, 2016.

[4] A. S. Fleischer, Thermal Energy Storage Using Phase Change Materials, Cham: Springer International Publishing, 2015.

[5] A. Sharma, V. V. Tyagi, C. R. Chen and D. Buddhi, "Review on thermal energy storage with phase change materials and applications," *Renewable and Sustainable Energy Reviews,* vol. 13, no. 2, pp. 318-345, 2009.

[6] A. A. Al-Abidi, S. Bin Mat, K. Sopian, M. Y. Sulaiman, C. H. Lim and A. Th, "Review of thermal energy storage for air conditioning systems," *Renewable and Sustainable Energy Reviews,* vol. 16, no. 8, pp. 5802-5819, 2012.

[7] M. Saffari, A. de Gracia, S. Ushak and L. Cabeza, "Economic impact of integrating PCM as passive system in buildings using Fanger comfort model," *Energy and Buildings,* vol. 112, pp. 159-172, 2016.

[8] D. Neeper, "Thermal dynamics of wallboard with latent heat storage," *Solar Energy,* vol. 68, no. 5, pp. 393-403, 2000.

[9] A. K. Sleiti and E. J. Naimaster, "Application of Fatty Acid Based Phase-Change Material to Reduce Energy Consumption From Roofs of Buildings," *Journal of Solar Energy Engineering,* vol. 138, no. 5, p. 051003, 2016.

[10] A. Athienitis, C. Liu, D. Hawes, D. Banu and D. Feldman, "Investigation of the thermal performance of a passive solar test-room with wall latent heat storage," *Building and Environment,* vol. 32, no. 5, pp. 405-410, 1997.

[11] K. Lin, Y. Zhang, H. Di and R. Yang, "Study of an electrical heating system with ductless air supply and shape-stabilized PCM for thermal storage," *Energy Conversion and Management,* vol. 48, no. 7, pp. 2016-2024, 2007.

[12] S. Li, G. Sun, K. Zou and X. Zhang, "Experimental research on the dynamic thermal performance of a novel triple-pane building window filled with PCM," *Sustainable Cities and Society,* vol. 27, pp. 15-22, 2016.

[13] T. Silva, R. Vicente, C. Amaral and A. Figueiredo, "Thermal performance of a window shutter containing PCM: Numerical validation and experimental analysis," *Applied Energy,* vol. 179, pp. 64-84, 2016.

[14] P. Schossig, H. Henning, S. Gschwander and T. Haussmann, "Micro-encapsulated phase-change materials integrated into construction materials," *Solar Energy Materials and Solar Cells,* vol. 89, no. 2-3, pp. 297-306, 2005.

[15] C. Voelker, O. Kornadt and M. Ostry, "Temperature reduction due to the application of phase change materials," *Energy and Buildings,* vol. 40, no. 5, pp. 937-944, 2008.

[16] F. Souafayne, F. Fardoun and P.-H. Biwole, "Phase change materials (PCM) for cooling applications in buildings: A review," *Energy and Buildings,* vol. 129, pp. 396-431, 2016.

[17] B. Zalba, J. M. Marin, L. F. Cabeza and H. Mehling, "Free-cooling of buildings with phase change materials," *International Journal of Refrigeration,* vol. 27, no. 8, pp. 839-849, 2004.

[18] A. Mosaffa, C. Infante Ferreira, F. Talati and M. Rosen, "Thermal performance of a multiple PCM thermal storage unit for free cooling," *Energy Conversion and Management,* vol. 67, pp. 1-7, 2013.

[19] M. Anisur, M. Kibria, M. Mahfuz, R. Saidur and I. Metselaar, "Cooling of air using heptadecane phase change material in shell and tube arrangement: Analytical and experimental study," *Energy and Buildings,* vol. 85, pp. 98-106, 2014.

[20] E. Osterman, V. Butala and U. Stritih, "PCM thermal storage system for 'free' heating and cooling of buildings," *Energy and Buildings,* vol. 106, pp. 125-133, 2015.

[21] S. Takeda, K. Nagano, T. Mochida and K. Shimakura, "Development of a ventilation systemfor granules containing phase change material," *Solar Energy,* vol. 77, pp. 329-338, 2004.

[22] K. Yanbing, J. Yi and Z. Yinping, "Modeling and experimental study on an innovative passive cooling system—NVP system," *Energy and Buildings,* vol. 35, no. 4, pp. 417-425, 2003.

[23] P. McKenna, W. Turner and F. D.P., "Geocooling with integrated PCM thermal energy storage in a commercial building," *Energy,* vol. 144, pp. 865-876, 2018.

[24] M. Helm, C. Keil, S. Hiebler, H. Mehling and C. Schwiegler, "Solar heating and cooling system with absorption chiller and low temperature latent heat storage: Energetic

performance and operational experience," *International Journal of Refrigeration,* vol. 32, no. 4, pp. 596-606, 2009.

[25] M. Helm, K. Hagel, W. Pfeffer, S. Hiebler and C. Schweigler, "Solar Heating and Cooling System with Absorption Chiller and Latent Heat Storage – A Research Project Summary," *Energy Procedia,* vol. 48, pp. 837-849, 2014.

[26] J. Belmonte, M. Izquierdo-Barrientos, P. Eguia, A. Molina and J. Almendros-Ibanez, "PCM in the heat rejection loops of absorption chillers. A feasibility study for the residential sector in Spain," *Energy and Buildings,* vol. 80, pp. 331-351, 2014.

[27] R. Tackett, "Case study: office building uses ice storage, heat recovery, and cold air distribution," *ASHRAE Transactions,* vol. 95, no. 1, pp. 1113-1121, 1989.

[28] C. Sohn, "Field performance of an ice harvester storage cooling system," *ASHRAE Transactions,* vol. 97, no. 2, pp. 1187-1193, 1991.

[29] E. Oro, A. de Garcia, A. Castell, M. Farid and L. Cabeza, "Review on phase change materials (PCMs) for cold thermal energy storage applications," *Applied Energy,* vol. 99, pp. 513-533, 2012.

[30] Y. Yau and B. Rismanchi, "A review on cool thermal storage technologies and operating strategies," *Renewable and Sustainable Energy Reviews,* vol. 16, no. 1, pp. 787-797, 2012.

[31] Y. Yau and S. Lee, "Feasibility study of an ice slurry-cooling coil for HVAC and R systems in a tropical building," *Applied Energy,* vol. 87, no. 8, pp. 2699-2711, 2010.

[32] S. Morgan and M. Krarti, "Field testing of optimal controls of passive and active thermal storage," *ASHRAE Transactions,* vol. 116, no. 1, pp. 134-146, 2010.

[33] A. Faghri and Y. Zhang, Transport Phenomena in Multiphase Systems, Amsterdam: Elsevier, 2006.

[34] T. L. Bergman, A. S. Lavine, F. P. Incropera and D. P. Dewitt, Fundamentals of Heat and Mass Transfer, 7th ed., Hoboken: Wiley, 2011.

[35] PureTemp, "PureTemp 15 Technical Data Sheet," 2020. [Online]. Available: http://www.puretemp.com/stories/puretemp-15-tds. [Accessed 1 December 2020].

[36] US Department of Energy, "Climate Zones," Office of Energy Efficiency and Renewable Energy, 2020. [Online]. Available: https://www.energy.gov/eere/buildings/climate-zones. [Accessed 30 11 2020].

[37] M. C. Baechler, T. L. Gilbride, P. C. Cole, M. G. Hefty and K. Ruiz, "High-Performance Home Technologies: Guide to Determining Climate Regions by County," U.S. Department of Energy, 2015.

[38] ASHRAE, *ASHRAE Standard 90.1-2019 - Energy Standard for Buildings Except Low-Rise Residential Buildings,* Atlanta, 2019.

[39] El Paso Electric Company, "Schedule No. 24 General Service Rate," 18 July 2017. [Online]. Available: https://www.epelectric.com/files/html/Rates_and_Regulatory/13_-_Rate_24_General_Service_Rate.pdf. [Accessed 30 November 2020].

[40] Florida Power & Light Company, "Business rates and clauses," June 2020. [Online]. Available: https://www.fpl.com/content/dam/fpl/us/en/rates/pdf/Business%20(Effective%20June%202020).pdf. [Accessed 30 November 2020].

[41] Orange and Rockland Utilities Inc, "Time-of-Use Rates," 2020. [Online]. Available: https://www.oru.com/en/save-money/energy-saving-programs/time-of-use. [Accessed 30 November 2020].

[42] J. Kosny, N. Shukla and A. Fallahi, "Cost Analysis of Simple Phase Change Material-Enhanced Building Envelopes in Southern U.S. Climates," US Department of Energy, 2013.